

Numerical simulation of bubble deformation and breakup under simple linear shear flows

Mitsuhiro Ohta^{1,1,*}, Tetsuya Ueta¹, Yozo Toei¹, Edwin Jimenez¹, Mark Sussman¹

Abstract

Numerical simulations are presented for the deformation and breakup of a bubble in liquids undergoing simple linear shear flow in a variety of regimes including the low Capillary number, moderate/high Reynolds number regime. Numerical results are obtained using a projection method for incompressible two-phase flow. The method represents interfaces using the sharp interface coupled level set and Volume-Of-Fluid (CLSVOF) method. To verify the CLSVOF numerical algorithm and provide a basis for comparison, computational results are also presented that compare with previous, more popular, drop deformation and rupture simulations. The numerical results reveal that the shear-induced bubble deformation and breakup process differs significantly from that of the analogous drop system under similar flow conditions. The first distinguishing factor for bubble breakup is that the magnitude of shear flow necessary for causing rupture is much larger than that in the drop system case. In other words, a larger Reynolds number is needed to induce bubble breakup. The second distinct feature of the bubble system versus the drop system is that the bubble does not maintain a stable deformed shape as the system parameters approach the critical “breakup” Reynolds number. It is asserted that the differences in morphology for a bubble undergoing breakup versus a drop in the same process can be attributed to the density and viscosity ratio of the corresponding two-phase flow systems. The critical conditions for bubble breakup with respect to the Reynolds and capillary numbers are determined for several cases.

Keywords: Bubble deformation, bubble breakup, shear flow, CFD

¹ 1. Introduction

Bubble dynamics in shear flow, including breakup, is critically important for various gas-liquid scientific and engineering processes. We refer the reader to the following experimental studies relating to bubble deformation in foaming processes, microfluidic devices, microbubbles in the blood circulation system,

*Corresponding author: m-ohta@tokushima-u.ac.jp

6 materials processing, pharmaceuticals, minerals engineering, bubble column re-
7 actor, underwater projectiles, polyethylene devolatilization, microfluidics, food
8 aeration, passive cyclonic separators, and cosmetics[7, 36, 4, 11, 12, 68, 13, 72,
9 5, 17, 71, 15, 16, 35, 52, 51, 21, 54]. In particular, it is the study of bubble de-
10 formation as it pertains to high-performance plastics applications that motivate
11 this work.

12 At the present, there is a large hole in the research regarding fundamental
13 bubble dynamics in a simple shear flow. There are no results, either experi-
14 mentally or numerically, in the low Capillary number ($Ca = \mu_m U / \sigma$), mod-
15 erate/high Reynolds number ($Re = \rho_m R U / \mu_m$) regimes. In this void, it is
16 impossible to do experiments unless one is in a microgravity environment. At
17 the same time, numerical algorithms must be designed in order to robustly and
18 accurately predict the tensile strength of a bubble in the low capillary, moderate
19 to high Reynolds number regime, in which ours is the first to be reliably used
20 for such a purpose.

21 This article presents computational studies of shear-driven deformation and
22 breakup of a bubble in insoluble viscous liquids. Studying bubble break-up,
23 in which we focus only on the balance of the wall driving force and bubble
24 surface tension force, via computation rather than experiments simplifies the
25 process of setting a combination of precise, simple shear flow conditions, low
26 Capillary number ($Ca = \mu_m U / \sigma$) conditions, moderate/high Reynolds' number
27 conditions ($Re = \rho_m R U / \mu_m$), low-density ratio, low viscosity ratios, and zero
28 buoyancy effects. We remark that previous controlled experimental studies on
29 shear-driven bubble deformation are restricted to the low Reynolds' number and
30 large capillary number regime[50, 5]. One reason is that buoyancy effects are
31 minimized in highly viscous liquids. On the other hand, many applications are
32 characterized by liquids in the moderate/high Reynolds' number regime. The
33 physical properties that distinguish bubble and drop studies are expressed in
34 terms of the density ratio $\lambda = \rho_b / \rho_m$ and the viscosity ratio $\eta = \mu_b / \mu_m$, where
35 ρ is the fluid density, μ is the viscosity and the subscripts "b" and "m" denote
36 the "bubble" or "drop" and the "matrix fluid", respectively. For a bubble in
37 an insoluble, viscous liquid, $\lambda \simeq 0$ and $\eta \simeq 0$, whereas most studies dealing with
38 a drop in an immiscible viscous liquid take $\lambda = 1$ and $\eta \simeq 1$.

39 In this work, we focus on identifying critical flow states numerically, in terms
40 of dimensionless quantities, that specify the extreme conditions at which a bub-
41 ble in shear flow first transitions from deformation to breakup. We validate our
42 numerical method by examining the sensitivity of the critical bubble deforma-
43 tion and break-up flow states with respect to the grid size. We also compare
44 with previous experimental results where the experimental data is available
45 (the high Capillary number low Reynolds' number regime). An advantage of
46 studying shear-driven bubble deformation and breakup computationally rather
47 than experimentally is that one can easily modify bubble/drop shape initial
48 conditions [39], the gravity force term[21], fluid physical properties, and the ge-
49 ometry of the (virtual) apparatus[16]. In our computations, the time-evolution
50 of the boundary between gas and liquid is tracked with a Coupled-Level-Set
51 and Volume-Of-Fluid (CLSVOF) sharp interface capturing algorithm [60, 62].

52 The rationale for the CLSVOF method is that the hybrid method represents
53 the (complex) gas-liquid interfaces with minimal volume loss (property of the
54 Volume-Of-Fluid method) and minimal error in the approximation of the sur-
55 face tension force (property of the Level-Set method). Our sharp interface
56 approach[62, 57, 27] enables us to simulate multiphase flows without artificially
57 giving the interface an empirical thickness.

58 We focus on determining critical physical conditions in which the breakup of
59 a bubble occurs in shear flow because it is important to identify the parameter
60 regimes in which a relatively simple system transitions from stable to unstable.
61 Specifically, we ascertain the critical Reynolds number (Re_c) corresponding to
62 the bubble breakup onset condition as a function of Ca .

63 In previous experimental or computational studies on the motion of bubble
64 deformation in a simple shear flow [5, 50, 36], only findings for bubble defor-
65 mation under very low Re number conditions ($Re \ll 1$) have been reported.
66 This is understandable since a low Reynolds number matrix fluid mitigates the
67 effect of gravity on distorting the comparison with the drop case. In the results
68 reported in [5], the $x - z$ cross section of the deforming bubble was close to
69 circular in their experiments. Also in the experiments in [5], the $x - z$ cross
70 section shows minimal overall bubble rise speed in the (very) viscous fluid in
71 comparison to the rate that the bubble deforms in the $y - z$ cross section. This
72 is expected since the experiments designed by [5] closely followed the following
73 basic assumptions: (i) “steady creeping flow with negligible inertial effects,” (ii)
74 “Incompressible Newtonian fluids,” (iii) “No buoyancy effects,” (iv) “No wall
75 effects.” In this work, we determine, for the first time, the critical Reynolds
76 number ($Re \gg 1$) that leads to bubble breakup. Additionally, our computa-
77 tional studies reveal characteristics that distinguish a drop’s deformation and
78 breakup processes versus those of a bubble.

79 We remark that there have been a number of computational articles on the
80 study of lift of slightly deformable bubbles[14, 31]. We reiterate, though, that
81 for bubble deformation and breakup in shear flows, only a few computational
82 articles exist: [70, 69, 53]. These previous studies mainly examined the dynamics
83 (e.g., rotation angle) of bubble deformation in shear flow. Concerning bubble
84 breakup, Wei et al. [70] presented one numerical result for a bubble breakup
85 process under the condition of Ca (capillary number) = 35. Sharifi et al[53]
86 presented two results for bubble breakup corresponding to $Ca = 7.5$ and $Ca =$
87 11.2. We point out that all of the previous computational research on bubble
88 deformation (and breakup) under shear driven flow[70, 69, 53] use the (explicit)
89 Lattice Boltzmann method. For accurately computing the tensile strength of a
90 bubble, and accurately computing threshold parameters for break-up (what we
91 do in this article, and what was not done in previous work), it is critical that a
92 numerical method directly enforces the velocity continuity condition and the gas-
93 liquid interface normal jump conditions. We contend that a projection method
94 (i.e. this paper and [74, 75, 41]) is the more appropriate (albeit slower) method
95 for our study rather than the Lattice Boltzmann method. Also, in contrast to
96 the Lattice Boltzmann method, our interface “capturing” method, the CLSVOF
97 method[60, 62], maintains the gas/liquid interface as sharp, enables accurate

98 approximation of the surface tension force, and by construction the CLSVOF
99 method preserves mass and volume within a fraction of a percent. The results
100 that we present in this article (see e.g. section 3.3.2) regarding measuring the
101 tensile strength of a bubble are unique and validated with respect to comparisons
102 with previous experimental data (where available) and grid refinement studies.
103 Each simulation on the finest resolution takes over a half a year to complete on
104 a workstation because of the following unavoidable factors: (i) the large density-
105 ratio projection method requires the solution of a large sparse, ill-conditioned,
106 matrix system at each time step, (ii) the finer the mesh, the more precise the
107 measured threshold, and right at the threshold (Taylor Deformation parameter
108 $D \approx 1$), oscillatory behaviour is observed delaying the determination of breakup
109 or not. Finally, the larger the deformation parameter D , the longer one must
110 make the computational domain (and thereby leading to larger domain aspect
111 ratio) thereby adversely effecting the condition number even more for carrying
112 our the pressure projection.

113 To highlight the mechanisms of bubble deformation and breakup in a shear
114 flow, we juxtapose the bubble results with those of a drop. We remark that
115 while the study of critical tensile strength parameters for the bubble is sparse,
116 there have been many studies for the simpler drop problem. This is because
117 the density ratio for the drop deformation case is almost one so that it is not
118 required that the continuous phase liquid be highly viscous in order to mitigate
119 buoyancy effects. For completeness, we give a brief overview of previous “tensile
120 strength” studies pertaining to drops.

121 The study of the deformation and breakup of a drop in immiscible vis-
122 cous liquids undergoing simple linear shear flow has been investigated exten-
123 sively due to its fundamental importance to emulsion processes, materials pro-
124 cessing, mixing, and reaction devices. The pioneering experimental work on
125 this problem was performed by Taylor in the early 1930s [65, 66], and the
126 subsequent theoretical and experimental progress up to the 1980s and 1990s
127 was reviewed in [43] and [56], respectively. By the 2000s, progress in com-
128 putational fluid dynamics (CFD) techniques and increased access to powerful
129 computing resources led to a surge of research focused on direct simulations
130 of this problem. In particular, detailed computational investigations of drop
131 breakup, based on a Volume-of-Fluid (VOF) method [20] were presented in
132 [33, 47, 49, 48, 28, 44, 45, 46]. Since then, the literature on computational stud-
133 ies on the deformation and breakup of a single or several drops in shear flow
134 has continued to grow [9, 23, 73, 3, 25, 10, 29, 30, 24, 19, 1, 76] and a variety
135 of numerical techniques have been developed to tackle this problem, including
136 boundary-integral approaches [8, 26], lattice Boltzmann methods [22, 29], front
137 tracking schemes [67], and interface-capturing level set methods [61].

138 Thus, a lot of studies about the deformation and breakup of a drop in simple
139 linear shear have been presented so far. In contrast, few studies have been
140 conducted on bubble deformation and breakup. In the low Capillary number,
141 moderate/high Reynolds’ number regime, there are no controlled experiments or
142 simulations. We reiterate why there have been few studies regarding the “tensile
143 strength” of bubbles. Experimentally, if one wants to isolate the interplay of

144 shearing force with the bubble surface tension force, in the moderate to high
 145 Reynolds number regime, and low Capillary number regime, one is restricted
 146 to microgravity conditions. Computational experiments are difficult too. In
 147 order to accurately compute the tensile strength of a bubble, one must resort
 148 to a combination of parallel computing, the multigrid preconditioned conjugate
 149 gradient method[64, 62] for poorly conditioned large sparse matrix systems,
 150 adaptive mesh refinement[77, 62], and a robust, volume preserving interface
 151 tracking method (we use the CLSVOF method[60, 62]). These aspects of our
 152 algorithm allow one to accurately simulate the balance of the restoring bubble
 153 surface tension force against the driving wall shear force and at the same time,
 154 accurately simulate the evolution of the bubble shape to bubble-break-up if the
 155 given shear stress and physical properties permit it.

156 2. Problem Description

157 Figure 1(a) shows a schematic of the computational system for our studies
 158 of a bubble (or drop) in shear flow. The computational domain consists of a
 159 three-dimensional rectangular domain with the dimensions of L (length) \times W
 160 (width) \times H (height). The size of L , W and H was determined after considera-
 161 tion of the sensitivity of numerical results to the domain size; numerical studies
 162 of domain-size dependence are presented in Section 3.3. All computational re-
 163 sults that follow were obtained from numerical solutions of the three-dimensional
 164 governing equations for gas-liquid/liquid-liquid flows. Computations are initial-
 165 ized with a spherical bubble (or drop) of radius $R = 5$ mm set at the center of
 166 the computational domain. The bubble (or drop) is then subjected to a linear
 167 shear flow generated by the motion of the top and bottom plates, which have
 168 constant velocity $+V$ and $-V$, respectively. In the interior of the domain, the
 169 initial velocity condition is assumed to be a simple linear profile and periodic
 170 boundary conditions are imposed along the x and y directions. Mathematically,
 171 the initial and boundary conditions are described as follows:

$$\phi(x, y, z, 0) = \sqrt{(x - \frac{L}{2})^2 + (y - \frac{W}{2})^2 + (z - \frac{H}{2})^2} - R \quad (1)$$

$$\mathbf{u}(x, y, z, 0) = \begin{pmatrix} \frac{2V}{H}(z - \frac{H}{2}) \\ 0 \\ 0 \end{pmatrix}$$

$$\phi(x + L, y, z, t) = \phi(x, y, z, t) \quad \phi(x, y + W, z, t) = \phi(x, y, z, t)$$

$$\mathbf{u}(x, y, H, t) = \begin{pmatrix} V \\ 0 \\ 0 \end{pmatrix} \quad \mathbf{u}(x, y, 0, t) = \begin{pmatrix} -V \\ 0 \\ 0 \end{pmatrix}$$

$$\mathbf{u}(x + L, y, z, t) = \mathbf{u}(x, y, z, t) \quad \mathbf{u}(x, y + W, z, t) = \mathbf{u}(x, y, z, t)$$

172 $\phi(x, y, z, t)$ is a material indicator function which is positive in the “matrix”
 173 fluid and negative in the bubble (or drop) fluid. $\mathbf{u}(x, y, z, t)$ is the velocity.

174 Common dimensionless physical parameters used to describe gas-liquid or
 175 liquid-liquid two-phase flows include the Reynolds (Re), Weber (We) (or Ca (=
 176 We/Re)) and Froude (Fr) numbers. Gas-Liquid and Liquid-Liquid two-phase
 177 flow problems are also determined by the density ratio λ and the viscosity ratio
 178 η . In the present study, in order to clearly isolate the effects of λ and η , and
 179 isolate the balance of the driving wall force with the bubble surface tension
 180 force, the effect of gravity is not considered ($g = 0$) so that we ignore the effect
 181 of the Fr number $\left(= \frac{\Gamma R}{\sqrt{gR}} \right)$.

182 When comparing with previous drop studies, we fix $\lambda = 1$ for the drop cases.
 183 As a result, (for $\lambda = 1$) the following dimensionless physical parameters are used
 184 to describe the problem of drop deformation/breakup in shear flow:

$$Re = \frac{\rho_m U R}{\mu_m}, \quad Ca = \frac{\mu_m U}{\sigma}, \quad \eta = \frac{\mu_b}{\mu_m} \quad m = \text{matrix fluid} \quad (2)$$

185 U is the velocity scale and σ denotes the surface tension. For the problem of
 186 shear-induced drop deformation and breakup, the velocity is set to,

$$U = \Gamma R,$$

187 where the shear-rate is,

$$\Gamma = 2V/H.$$

188 As mentioned in the introduction, most previous drop studies set $\eta = 1$ (e.g. Li
 189 et al. [33]). Thus, for comparison with previous drop deformation and breakup
 190 problems, we set $\lambda = \eta = 1$ (and also neglect the effect of gravity so that
 191 $g = 0$). On the other hand, in our computations for bubble deformation, we
 192 set the density and viscosity of air to be $\rho_b = 1.2 \text{ kg/m}^3$ and $\mu_b = 1.8 \times 10^{-5}$
 193 Pa·s respectively. We emphasize that for consistency with previous studies (Li
 194 et al. [33], Rust and Manga [50], Müller-Fischer et al. [36], Komrakova et al.
 195 [29], Amani et al. [1]), we computationally examine the deformation and breakup
 196 of a bubble in simple linear shear flow as a function of the Re and Ca numbers.
 197 That is to say, by setting $g = 0$, we are isolating the effect of only varying Re and
 198 Ca on bubble deformation and breakup. In our controlled study, we determine
 199 the critical Re_c versus Ca curve in which Re_c corresponds to the threshold of
 200 bubble (or drop) breakup. We determine the critical Re_c versus Ca curve for
 201 strategic pairs of the density ratio and viscosity ratio.

202 In our computations, the density of the matrix fluid is fixed at $\rho_m = 1000$
 203 kg/m^3 . The surface tension at the bubble (drop) interface is $\sigma = 2.5 \times 10^{-2}$
 204 N/m. The values of Re and Ca in our simulations are controlled by changing
 205 the values of μ_m and V . Specifically, we set $\mu_m = 2.0 \times 10^{-2} \sim 6.0 \times 10^{-2}$
 206 Pa·s and $V = \text{about } 1.1 \sim 1.3 \text{ m/s}$. As a consequence, for studying bubble
 207 deformation and break-up, the density and viscosity ratios satisfy $\lambda = 1.2 \times 10^{-3}$
 208 and $\eta < 1.0 \times 10^{-3}$.

209 Remark: if we were to apply “Earth” gravity conditions in our simulations,
 210 then $g = 9.8 \text{ m/s}^2$, and the Froude number (Fr) is in the range $Fr = 1.7 \sim 1.9$.

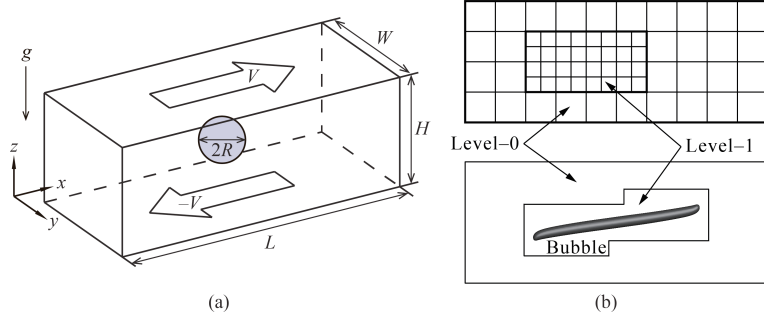


Figure 1: (a) Computational domain schematic for a bubble or drop in shear flow. Gravity is set to zero in our computations in order to isolate the effects of density and viscosity ratios. (b) (upper panel) a two-level adaptive mesh refinement (AMR) grid schematic corresponding to one of our simulations; (lower panel) snapshot of bubble deformation in simple linear shear flow.

211 Although these values of Fr are not so large, the effect of gravity (inducing
 212 bubble rise motion) may not be completely negligible. However, bubbles in
 213 our computations reach the breakup by way of deformation very quickly at t
 214 = about 0.5 s. Accordingly, it is expected that the effect of gravity (inducing
 215 bubble rise motion) can be small for the behavior of bubble deformation and
 216 breakup around the critical Re number conditions determined in our study.

217 3. Numerical Analysis

218 3.1. Numerical method and governing equations

219 Numerical results were obtained using the interface capturing Coupled Level
 220 Set and Volume of Fluid (CLSVOF) method (Sussman and Puckett [60], Suss-
 221 man et al. [62]), which is based on a fixed grid finite volume algorithm. The
 222 CLSVOF method is a robust numerical technique that combines some of the ad-
 223 vantages of the Volume of Fluid (VOF) method (Hirt and Nichols [20]) and the
 224 Level Set (LS) (Sussman et al. [61]) method while overcoming their weaknesses.
 225 In the VOF method, the Volume Fraction function, F , is used to represent
 226 the interface. The values of F correspond to the volume fraction of liquid in
 227 a given computational cell. In other words, $F = 0$ when a computational cell
 228 contains only gas and $F = 1$ when a computational cell contains only liquid.
 229 If $0 < F < 1$, then a computational cell contains the gas-liquid interface. The
 230 VOF method has an advantage over the LS method in that accurate algorithms
 231 for advecting F can be applied so that mass/volume is conserved up to machine
 232 precision while still maintaining a sharp representation of the interface. On
 233 the other hand, the disadvantage of the VOF method in comparison to the LS
 234 method is that tangled and difficult reconstruction procedures are required for
 235 determining the slope of the piecewise linear VOF reconstructed interface. In
 236 the LS method, the signed distance function ϕ (LS function) is used to track the
 237 interface. The interface is implicitly represented by the set of points in which

238 $\phi = 0$. Liquid and gas regions are defined as $\phi > 0$ in the liquid and $\phi < 0$ in the
 239 gas, respectively. One of the advantages of the LS method is that one can track
 240 and represent smoothly the interface, but the LS method has the disadvantage
 241 that mass/volume is not explicitly conserved. In the CLSVOF method, the cou-
 242 pling between the LS function and the VOF function occurs when computing
 243 the normal of the reconstructed interface in the VOF calculation process and
 244 also when assigning the LS function with the exact signed normal distance to
 245 the reconstructed interface in the LS calculation process. That is to say, the
 246 piecewise linear approximation (the volume-of-fluid reconstruction step) for the
 247 VOF method is determined using the unit normal vector (\mathbf{n}) estimated from
 248 information of the LS function. By taking advantage of both methods, the evo-
 249 lution of the liquid-gas interface location can be computationally captured in
 250 such a way so that volume/mass is preserved to machine precision and at the
 251 same time, the interface normals and the surface tension force (which is pro-
 252 portional to the interface curvature) can be straightforwardly derived from the
 253 smooth level set function.

254 In our studies, the two-phase fluid flow is comprised of air and a viscous
 255 Newtonian liquid. The Heaviside function, $\mathcal{H}(\phi)$, which is defined as

$$\mathcal{H}(\phi) = \begin{cases} 1 & \phi \geq 0 \\ 0 & \phi < 0 \end{cases} \quad (3)$$

will be used below to distinguish each of the two fluids. A single set of three-dimensional equations governs the motion of both fluids, which are taken to be incompressible, and consists of the continuity equation and the Navier-Stokes equations with surface tension forces:

$$\nabla \cdot \mathbf{u} = 0 \quad (4)$$

$$\frac{\partial \mathbf{u}}{\partial t} + (\mathbf{u} \cdot \nabla) \mathbf{u} = \frac{1}{\rho} \nabla \cdot (-p \mathbf{I} + 2\mu \mathbf{D}) + \mathbf{g} - \frac{\sigma \kappa}{\rho} \nabla \mathcal{H} \quad (5)$$

256 We note that our method is a “sharp interface method[62, 57, 27]. Thereby
 257 we do not need to specify an empirical interface thickness parameter[61, 60].

258 \mathbf{u} is the velocity vector, t represents time, p is the pressure, \mathbf{I} is the unit ten-
 259 sor, \mathbf{D} is the rate of deformation tensor ($\mathbf{D} = \frac{1}{2}(\nabla \mathbf{u} + (\nabla \mathbf{u})^T)$), ρ is the density,
 260 μ is the viscosity, κ is the interfacial curvature, and the Heaviside function $\mathcal{H}(\phi)$
 261 is a function of the level set (LS) function ϕ . The singular Heaviside gradient
 262 term in the right-hand side of equation (5) is a body force representing the sur-
 263 face tension force and is equivalent to specifying that the jump in the normal
 264 stress is equal to $\sigma \kappa$ (Tanguy et al. [63]). The surface tension force expressed by
 265 the singular Heaviside gradient term acts only on the gas-liquid interface. The
 266 sharp interface “Ghost Fluid Method” (Kang et al. [27]) is used to discretize
 267 the gradient of the Heaviside function as it appears in the surface tension force
 268 term. This force, upon discretization, is only non-zero across cells in which the
 269 level set function changes sign.

270 The interfacial curvature κ is computed with second-order accuracy directly
 271 from the volume-of-fluid (VOF) function and the level set function using the

²⁷² height function technique (Sussman [57], Sussman et al. [62]). We note that we
²⁷³ would get the same results if we compute κ directly from the LS function using
²⁷⁴ the “level set” height function technique.

²⁷⁵ Since ρ and μ are taken to be constant in each fluid, with a jump at the
²⁷⁶ interface, they can be expressed in terms of the Heaviside function,

$$\rho = \rho_m \mathcal{H} + \rho_b (1 - \mathcal{H}), \quad \mu = \mu_m \mathcal{H} + \mu_b (1 - \mathcal{H}). \quad (6)$$

The subscripts “b” and “m” refer to “bubble” (or drop) and “matrix fluid.” To represent the free surface with the CLSVOF method, we must evolve the solution to both the VOF equation for F and the LS equation for ϕ :

$$\frac{\partial F}{\partial t} + (\mathbf{u} \cdot \nabla) F = 0, \quad \frac{\partial \phi}{\partial t} + (\mathbf{u} \cdot \nabla) \phi = 0. \quad (7)$$

²⁷⁷ In all computations, the discretized variables p , ϕ , and F are located at the
²⁷⁸ cell centers, and the discrete velocity variable \mathbf{u} is located at the cell face cen-
²⁷⁹ ters. Our computations are performed using an overall second-order accurate
²⁸⁰ hydrodynamic scheme. The spatial discretization uses second-order accurate,
²⁸¹ slope-limited, upwind techniques for the nonlinear advective terms. The ve-
²⁸² locity and pressure fields are computed using an implicit pressure projection
²⁸³ procedure.

²⁸⁴ The temporal discretization of our numerical method is an operator split
²⁸⁵ projection method as described by Sussman et al. [62]. An outline of our method
²⁸⁶ is as follows (see Sussman et al. [62], section 4, for more details):

All Steps. Timestep

²⁸⁷ The timestep, Δt , is governed by the CFL condition and surface tension
²⁸⁸ (section 5.7 of Sussman et al. [62]):

$$\Delta t < \min_{i,j,k} \left(\frac{\Delta x}{2|U^n|}, \frac{1}{2} \sqrt{\frac{\rho^L}{8\pi\sigma}} \Delta x^{3/2} \right)$$

Step 1. CLSVOF interface advection

$$\begin{aligned} \phi^{n+1} &= \phi^n - \Delta t [\mathbf{u} \cdot \nabla \phi]^n \\ F^{n+1} &= F^n - \Delta t [\mathbf{u} \cdot \nabla F]^n \end{aligned}$$

Step 2. Nonlinear advective force terms

$$\mathcal{A} = [\mathbf{u} \cdot \nabla \mathbf{u}]^n$$

Step 3. Viscosity force

$$\frac{\mathbf{u}^* - \mathbf{u}^n}{\Delta t} = -\mathcal{A} + g\vec{z} - [\nabla p/\rho]^n + \frac{1}{2} \frac{\nabla \cdot (2\mu \mathbf{D}^n) + \nabla \cdot (2\mu \mathbf{D}^*)}{\rho}$$

²⁸⁹ **Step 4. Pressure projection and ghost fluid surface tension algorithm**

$$\mathbf{V} = \mathbf{u}^n + \Delta t(-\mathcal{A} + g\vec{z} + \frac{1}{2} \frac{\nabla \cdot (2\mu \mathbf{D}^n) + \nabla \cdot (2\mu \mathbf{D}^*)}{\rho})$$

²⁹⁰

$$\mathbf{V} = \mathbf{V} - \Delta t \frac{\sigma \kappa(\phi^{n+1})}{\rho} \nabla \mathcal{H}(\phi^{n+1})$$

²⁹¹

$$\nabla \cdot \frac{\nabla p}{\rho} = \frac{1}{\Delta t} \nabla \cdot \mathbf{V}$$

²⁹²

$$\mathbf{u}^{n+1} = \mathbf{V} - \Delta t \frac{\nabla p}{\rho}$$

²⁹³ To make efficient use of computational resources, our numerical simulations
²⁹⁴ utilize an adaptive hierarchy of grids based on a dynamic adaptive mesh refine-
²⁹⁵ ment (AMR) technique (Sussman et al. [58]). Adaptive grids are dynamically
²⁹⁶ adjusted based on the location of the deforming gas-liquid interface. In the
²⁹⁷ AMR technique, the grid resolution is increased in regions near the interface,
²⁹⁸ while a coarser grid is used where the flow is relatively steady. The upper panel
²⁹⁹ of Figure 1(b) displays a schematic view of the hierarchical grid structure, and
³⁰⁰ the lower panel corresponds to an actual computational example corresponding
³⁰¹ to bubble deformation in simple linear shear flow. In general, the mesh hier-
³⁰² archy is composed of different levels of refinement ranging from coarsest $\ell = 0$
³⁰³ (“level-0”) to finest $\ell = \ell_{\max}$ (“level- ℓ_{\max} ”). The refinement ratio of one grid
³⁰⁴ size ($\Delta x = \Delta y = \Delta z$) to the next finer level is two so that $\Delta x^{\ell+1} = 0.5 \Delta x^\ell$. All
³⁰⁵ computations in this study used an AMR system with a maximum prescribed
³⁰⁶ level $\ell_{\max} = 1$ (as illustrated in the upper panel of Figure 1(b)). In our adaptive
³⁰⁷ mesh refinement algorithm, the velocity in the coarse grid cells that neighbor
³⁰⁸ fine grid cells are interpolated from the coarse grid using bilinear interpolation to
³⁰⁹ initialize “ghost” fine cells. Thus, the bilinear interpolation procedure produces
³¹⁰ interpolated fine-grid data as a linear combination of the coarse-grid data.

³¹¹ **Remark 1:** Due to time step stability constraints, the variable density pres-
³¹² sure projection process, and computed bubble shapes with high aspect ratio,
³¹³ we find that our simulations can take over six months. We have experimented
³¹⁴ with (a) decreasing the “error buffer” parameter from two cells to one (radius
³¹⁵ of cells to be tagged when a given cell is tagged for adaptivity) and (b) relaxing
³¹⁶ the condition that the bubble-liquid interface be wholly contained on the finest
³¹⁷ adaptive level. Unfortunately, we have found that these steps lead to poorer
³¹⁸ accuracy. This “diminishing returns” phenomenon is expected for low Mach
³¹⁹ number flows in which the incompressible flow equations are characterized by
³²⁰ non-local behavior. We refer the reader to the following research[34] in which
³²¹ it has been found through a systematic study that using an AMR grid can be
³²² less accurate than a case with a uniform fine grid (luckily, that is not the case

here). To summarize, we have found that each further refinement of the grid will multiply the simulation time by about eight (a factor of 4 due to spatial refinement and a factor of 2 due to temporal refinement).

Remark 2: We believe that including a customized sub-scale model right at the point of bubble break-up is unnecessary because the driving shear force is uniformly applied in the time variable instead of impulsively applied. We are aware of research for predicting whether droplets merge or bounce[32] that necessitate the inclusion of a sub-scale model, but that research is not applicable in our case. Previous studies on the shear flow-driven breakup of bubbles or drops have not incorporated customized subscale models[33, 29, 1].

3.2. Validation of the numerical method

The effectiveness of our sharp interface computational method has been demonstrated via grid refinement studies and comparison with experiments for the complicated rising motion of single bubbles and drops in viscous liquids Ohta and Sussman [41], Ohta et al. [37, 38, 42], Stewart et al. [55], Sussman et al. [62], Sussman and Ohta [59], the simulation of atomization in a realistic diesel injector[2], and the simulation of bubble formation due to the injection of gas through a nozzle[40]. In this section, the accuracy of our computational method will be verified for the problem of shear-induced deformation of a drop and bubble.

First, we compare quantitatively against the steady-state drop deformation results reported by Li et al. [33]. The shape of a deformed drop in simple linear shear flow is described in terms of the Taylor deformation parameter $D=(a-b)/(a+b)$, where a and b are the major and minor axes of the deformed drop, respectively. For consistency, we perform numerical simulations using CLSVOF over the same computational domain and grid size used in Li et al. [33], which has dimensions $L(8R) \times W(4R) \times H(8R)$ (recall that R is the bubble/drop radius) and a level-0 grid size $\Delta x = \Delta y = \Delta z = R/8$; our two-level AMR grid structure also uses a finer level-1 grid size $\Delta x^{\ell=1} = \Delta y^{\ell=1} = \Delta z^{\ell=1} = R/16$. Numerical results are listed in Table 1 for D as a function of Re , with $Ca = 0.3$ and $\lambda = \eta = 1$ fixed in every case. The results in Table 1 compare computations using our CLSVOF algorithm with corresponding results obtained with the VOF method used in Li et al. [33].

Table 1: Comparison of the Taylor deformation parameter D for a drop as a function of Re ($Ca = 0.3$, $\lambda = \eta = 1$). In all cases, the domain size is $L(8R) \times W(4R) \times H(8R)$, where R is the drop radius. The CLSVOF method computations used a two-level AMR computational domain with a level-0 discretization $\Delta x^{\ell=0} = \Delta y^{\ell=0} = \Delta z^{\ell=0} = R/8$ and a level-1 discretization $\Delta x^{\ell=1} = \Delta y^{\ell=1} = \Delta z^{\ell=1} = R/16$.

Reynolds number	0.1	0.5	0.6	0.75
D (Li et al. [33])	0.3968	0.45	0.4768	Breakup
D (Our study)	0.3960	0.4570	0.4758	Breakup

355

Next, we report the results of validation tests conducted with our computational method; we compare our results with the “bubble deformation in simple linear shear flow” results reported by Müller-Fischer et al. [36]. Müller-Fischer et al. [36] experimentally inquired into the bubble deformation under the condition of $Re \approx 0$. In our study, we computed the bubble deformation on a computational domain with dimensions $L(12R) \times W(6R) \times H(6R)$ and a computational grid in which the finest level grid size was $\Delta x^{\ell=1} = \Delta y^{\ell=1} = \Delta z^{\ell=1} = R/16$. Computations were performed for the conditions of $Ca = 0.96$ and $Ca = 1.63$ with $Re \approx 0$ ($Re = 5.0 \times 10^{-4}$), $\lambda = 1.2 \times 10^{-3}$ and $\eta \leq 1.2 \times 10^{-6}$. The prescribed parameters are consistent with the experimental conditions by Müller-Fischer et al. [36]. Comparisons of our numerical results and previous experimental results (Müller-Fischer et al. [36]) are tabulated in Table 2. Additionally, in Table 2, we list experimental results with the condition of $Re \approx 0$ and $\lambda \approx \eta \approx 0$ by Rust and Manga [50]. These experimental values were obtained from the graph showing the relation of D vs Re (Rust and Manga [50]). As is clear from Table 2, our numerical results predicted larger values of D than experimental ones reported by Müller-Fischer et al. [36]. Nevertheless, our numerical results are very close to the experimental results by Rust and Manga [50], which emphasizes the intrinsic difficulties associated with experimental investigations of bubble dynamics, even in simple linear shear flow. These comparisons suggest that our computational method is effective and robust at reproducing bubble dynamics in simple linear shear flow.

Table 2: Comparison of D for a bubble as a function of Ca ($Re \approx 0$, $\lambda \approx \eta \approx 0$). In all cases, the domain size is $L(12R) \times W(6R) \times H(6R)$. The CLSVOF computations used a two-level AMR computational domain with a level-0 discretization $\Delta x^{\ell=0} = \Delta y^{\ell=0} = \Delta z^{\ell=0} = R/8$ and a level-1 discretization $\Delta x^{\ell=1} = \Delta y^{\ell=1} = \Delta z^{\ell=1} = R/16$.

Capillary number	0.96	1.63
D (Müller-Fischer et al. [36])	0.37	0.58
D (Rust and Manga [50])	0.71 ± 0.05	0.81 ± 0.02
D (Our study $\Delta x^{\ell=1} = R/16$)	0.63	0.71

Finally, we compare numerical results from our method with the numerical results for drop breakup reported in Renardy and Cristini [49]. Figure 2 demonstrates drop breakup with pinch-off behavior for three Re and Ca conditions and with constant values of $\lambda = \eta = 1$ for all cases. The three cases that we consider correspond to (a) $Re = 10$, $Ca = 0.16$, (b) $Re = 12$, $Ca = 0.1753$, and (c) $Re = 15$, $Ca = 0.196$, and which are illustrated in Figures 2(a)-(c), respectively. The results reported in Renardy and Cristini [49], which were obtained with a VOF method, are shown inside boxes while results obtained with our CLSVOF approach are displayed outside boxes. In the computations presented in Renardy and Cristini [49], the dimensions $W = 4R$ and $H = 8R$ were fixed, while L was changed depending on Re and Ca conditions, and the grid size was set to $\Delta x = \Delta y = \Delta z = R/8$. To compare with their results, we performed simulations with the CLSVOF method over a two-level

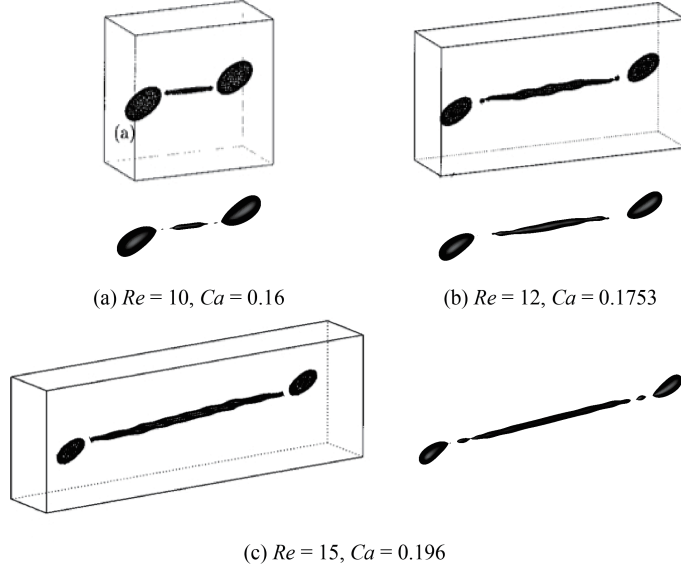


Figure 2: Comparison with results reported in Renardy and Cristini [49] (shown in bounding boxes) for drop breakup in shear flow. In Renardy and Cristini [49], the computational domain dimensions were $W = 4R$, $H = 8R$, and L was varied depending on the Re and Ca conditions. The grid size in Renardy and Cristini [49] was set to $\Delta x = \Delta y = \Delta z = R/8$. Reprinted with permission from reference Renardy and Cristini [49]. Copyright 2001, AIP Publishing. The results obtained with our CLSVOF algorithm, corresponding to each case in reference Renardy and Cristini [49], are shown without the bounding boxes. The CLSVOF method used a two-level AMR computational domain with a level-0 discretization $\Delta x^{\ell=0} = \Delta y^{\ell=0} = \Delta z^{\ell=0} = R/8$ and a level-1 discretization $\Delta x^{\ell=1} = \Delta y^{\ell=1} = \Delta z^{\ell=1} = R/16$. The onset of drop breakup is demonstrated for (a) $Re = 10$, $Ca = 0.16$, (b) $Re = 12$, $Ca = 0.1753$, and (c) $Re = 15$, $Ca = 0.196$. For all three Re and Ca conditions, $\lambda = \eta = 1$.

391 AMR computational domain of the same dimensions and the same level-0 dis-
 392 cretization: $\Delta x^{\ell=0} = \Delta y^{\ell=0} = \Delta z^{\ell=0} = R/8$; we set the finer level-1 grid size
 393 $\Delta x^{\ell=1} = \Delta y^{\ell=1} = \Delta z^{\ell=1} = R/16$. The results shown in Figure 2 verify that our
 394 numerical approach can reproduce the same drop breakup behavior presented
 395 in Renardy and Cristini [49]. Slight differences between the results can be at-
 396 tributed to the increased resolution used in our study in the level-1 grid around
 397 the elongated drop.

398 The numerical validation studies performed in this section and the follow-
 399 ing section demonstrate that our numerical method can reliably determine the
 400 transition regions at which shear-induced bubble or drop deformation leads to
 401 breakup. In the next section, we demonstrate that we can expect an error of 3%
 402 for predicting the transition to break-up. The analysis in this section and the
 403 following also indicate that the error is reduced by a factor of 2 each time the
 404 grid is refined by a factor of 2. We reiterate that we have found at least a factor
 405 of 2 error reduction for each grid refinement in many multiphase flow problems
 406 involving complex interface deformation and breakup; see Ohta and Sussman

407 [41], Ohta et al. [37, 38, 42], Stewart et al. [55], Sussman et al. [62], Arienti et al.
 408 [2], Ohta et al. [40].

409 *3.3. Consideration of domain and grid sizes*

410 *3.3.1. Selecting the appropriate domain size*

411 The computational domain size used in numerical studies can affect the
 412 behavior of drop deformation and breakup. Referring to Figure 1(a), with an
 413 appropriately large domain length L and a fixed width $W = 4R$, the effect of
 414 the height H on drop behavior was examined in Li et al. [33] for Stokes flows
 415 and various Ca conditions and in Komrakova et al. [29] for $Re = 1$ and $Ca =$
 416 0.27. Other related studies investigated drop breakup sensitivity (Renardy and
 417 Cristini [47]) and drop deformation sensitivity (Renardy et al. [48]) with respect
 to the entire domain size. Here, we investigate the drop dynamics sensitivity

Table 3: Comparison of the Taylor deformation parameter D for a drop as a function of domain size ($Re = 0.75$, $Ca = 0.3$, $\lambda = \eta = 1$). CLSVOF method computations used a two-level AMR computational domain with a level-0 discretization $\Delta x^{\ell=0} = \Delta y^{\ell=0} = \Delta z^{\ell=0} = R/8$ and a level-1 discretization $\Delta x^{\ell=1} = \Delta y^{\ell=1} = \Delta z^{\ell=1} = R/16$.

System	Domain size ($L \times W \times H$)	D
System 1	$8R \times 4R \times 8R$	Breakup
System 2	$12R \times 4R \times 8R$	Breakup
System 3	$8R \times 4R \times 6R$	0.541
System 4	$8R \times 6R \times 6R$	0.466
System 5	$8R \times 8R \times 8R$	0.460
System 6	$8R \times 16R \times 16R$	0.460

418 to domain size around the critical Reynolds number $Re_c = 0.75$. Specifically,
 419 we consider domain size sensitivity for the condition of $Re = 0.75$, $Ca = 0.3$,
 420 and $\lambda = \eta = 1$, a condition used in the comparison studies of the previous
 421 section. As shown in Table 1, the drop breaks up for the condition of $Re = 0.75$
 422 and $Ca = 0.3$ with a domain size of $L(8R) \times W(4R) \times H(8R)$. Results for
 423 domain size sensitivity for six domain systems, all of which use a level-1 grid
 424 size $\Delta x^{\ell=1} = \Delta y^{\ell=1} = \Delta z^{\ell=1} = R/16$, are tabulated in Table 3. Note that the
 425 domain size used in the comparison study (Table 1) corresponds to System 1.
 426

427 The results in Table 3 suggest that drop deformation is promoted when we
 428 use a domain size with $W = 4R$. In contrast, the drop does not break up and
 429 becomes stable with a deformed shape if we set L large enough and $W \geq 6R$ and
 430 $H \geq 6R$. Since the value of D for the domain size $L(8R) \times W(6R) \times H(6R)$ differs
 431 by only 1.3% with the value for the domain size of $L(8R) \times W(16R) \times H(16R)$,
 432 in the results that follow we set the width to $W = 6R$ and the height to $H = 6R$
 433 to minimize the number of computational grid nodes along those directions. To
 434 determine the critical Reynolds number Re_c (with $Ca = 0.3$), we consider a
 435 domain size of $L(24R) \times W(6R) \times H(6R)$, and we find that the drop reaches a
 436 stable state with deformation parameter $D=0.549$ for $Re = 1.0$, while a value
 437 of $Re = 1.1$ leads to drop breakup.

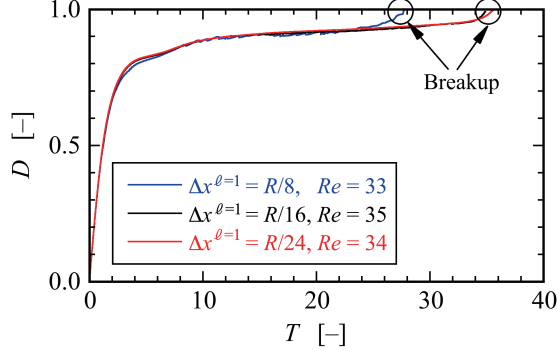


Figure 3: Time evolution of the deformation parameter D versus dimensionless time $T = \Gamma t$ for a bubble, obtained with three grid systems at different resolutions. All three resolutions use a two-level AMR grid with an effective fine resolution grid size $\Delta x^{\ell=1} = \Delta y^{\ell=1} = \Delta z^{\ell=1}$. The evolution of D using the first system, where $\Delta x^{\ell=1} = R/8$, is shown in blue and it predicts that bubble breakup occurs at a Reynolds number $Re = 33$. The evolution of D using the second system, where $\Delta x^{\ell=1} = R/16$, is shown in black and it predicts that bubble breakup occurs at a Reynolds number $Re = 35$. Results with the third system, shown in red, use $\Delta x^{\ell=1} = R/24$, and they predict that breakup occurs at $Re = 34$. The capillary number corresponding to these results is $Ca = 1.0$. ($\lambda = 1.2 \times 10^{-3}$, $\eta < 1.0 \times 10^{-3}$)

438 3.3.2. Selecting the appropriate grid size

439 The grid size and adaptive meshing strategy we adopt are chosen to answer
 440 the research question as to the conditions that determine whether a bubble in
 441 shear flow will break up. In such a case, we must accurately capture the balance
 442 of forces between the (non-local) force exerted from the wall-driven flow acting
 443 against the interfacial surface tension force. The accuracy of the “Critical
 444 Reynolds Number” depends on the largest Taylor Deformation parameter D
 445 that is supported by the grid (see e.g., Figures 8 and 11). As we report here,
 446 we have found that as long as the grid size is fine enough to support a Taylor
 447 Deformation parameter $D < 0.95$, then the transition region (i.e. “Critical
 448 Reynolds number”) (see Figures 3 and 12) will be captured with a tolerance
 449 of three percent. The simulation time would become impractical if we were
 450 to try further to improve the accuracy of the “critical Reynolds number”. A
 451 smaller tolerance would necessitate a larger supported Deformation parameter
 452 D , which would in turn, necessitate a higher aspect ratio computational domain,
 453 increased droplet surface area at break-up, increased number of time steps, and
 454 higher resolution for representing the drop/bubble at its thinnest point.

455 We distinguish between our present research and the research found in the
 456 work of Zhang et al. [74, 75] on predicting the conditions for bubble mergers.
 457 Even in the most extreme cases for mergers, the largest Deformation
 458 parameter never exceeds 0.4 in Zhang et al. [74]. In summary, our gridding
 459 requirements necessitate grid points distributed relatively evenly throughout the
 460 computational domain when a bubble is stretched to a $D = 0.9$ Deformation,
 461 whereas in Zhang et al. [74], the gridding strategy necessitates a more localized

462 approach.

463 The numerical results presented in this and the previous section used a
464 finest-level grid size set to $\Delta x^{\ell=1} (= \Delta y^{\ell=1} = \Delta z^{\ell=1}) = R/16$. To verify the
465 adequacy of this grid resolution, we present grid refinement results for a bubble
466 breakup simulation with $Ca = 1.0$, which corresponds to the most deformable
467 and stretchable bubble case considered in our numerical studies. We use three
468 different grid systems, (i) $\Delta x^{\ell=1} = R/8$, (ii) $\Delta x^{\ell=1} = R/16$, and (iii) $\Delta x^{\ell=1} =$
469 $R/24$, in order to determine Re_c . Figure 3 shows the time evolution of the
470 deformation parameter D over time for the three grid systems; the x -axis is a
471 dimensionless time defined by $T = \Gamma t$ and the y -axis is D . The results show that
472 bubble breakup occurs at $Re_c = 35$ for the grid system with $\Delta x^{\ell=1} = R/16$,
473 while the finer computational grid with $\Delta x^{\ell=1} = R/24$ predicts a critical value of
474 $Re_c = 34$. For the $\Delta x^{\ell=1} = R/8$ results, it is clear that the $R/8$ resolution is too
475 coarse to capture the proper break-up time, albeit the critical Reynolds' number,
476 $Re_c = 33$, was still close to the finer grid resolution cases. Note that although
477 the time evolution of D for the two finer resolution systems ($R/16$ and $R/24$)
478 is consistent between the two (the predicted critical Reynolds numbers differ
479 by $\sim 3\%$), the computational time using the grid system with $\Delta x^{\ell=1} = R/24$
480 was more than 6 times longer than the one based on the coarser system with
481 $\Delta x^{\ell=1} = R/16$. We remark that in our search for Re_c , we considered a wide
482 range of values of Ca , and we found it necessary to use a large L ($\sim 24R$) since
483 for certain shear flows the bubble can stretch significantly without breaking up.
484 Nevertheless, for the conditions presented in this section, the results indicate
485 that our numerical approach, even with a finest-level resolution set to $\Delta x^{\ell=1} =$
486 $R/16$, is capable of accurately reproducing bubble deformation and breakup
487 without sacrificing any essential dynamical features.

488 **4. Results and Discussion**

489 *4.1. Drop deformation and breakup*

490 To illustrate the differences in deformation and breakup between a drop
491 and a bubble around critical conditions, we first present numerical results for
492 drop deformation. The time evolution of drop deformation and breakup in
493 simple linear shear flow for two conditions is shown in Figure 4.1; the first case,
494 shown in Figure 4.1(a), uses $Ca = 0.3$ and $Re = 1.0$, while the second case,
495 depicted in Figure 4.1(b), uses $Ca = 0.3$ and $Re = 1.1$. Using a domain size
496 of $L(24R) \times W(6R) \times H(6R)$, in the case with $Re = 1.0$, the drop gradually
497 deforms and finally attains a stable deformed state.

498 After $T = 35.0$, the drop remains a stable deformed state with $D = 0.549$.
499 Over the same domain, for the case with $Re = 1.1$, the “mother” drop elongates
500 over time, and the volume at the ends of the deforming drop expands; both ends
501 become bulb-shaped. As time progresses, particularly over the time interval
502 $48.4 \leq T \leq 55.2$, a thread-bridge forms between the bulbous ends, and the
503 thread-bridge becomes thinner. Finally, at around the dimensionless time $T \sim$
504 56.7, the mother drop breaks up, forming two “daughter” drops through the

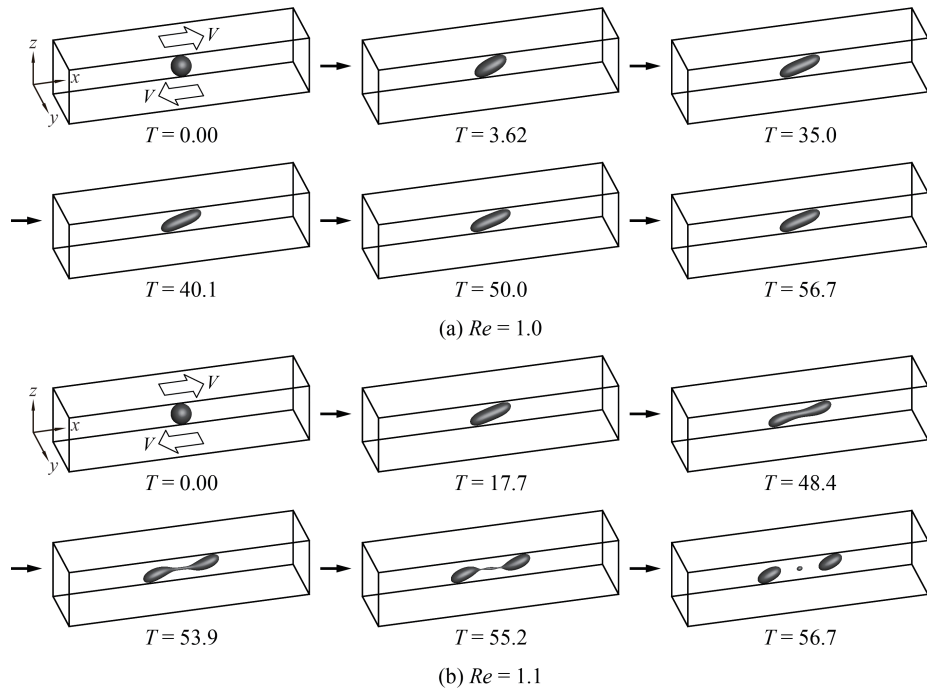


Figure 4: Time evolution of drop deformation and breakup in shear flow at the condition of $Ca = 0.3$ with (a) $Re = 1.0$ and (b) $Re = 1.1$. The “drop” critical Reynolds number corresponding to $Ca = 0.3$ is $1.0 < Re_c < 1.1$. ($\lambda = \eta = 1.0$)

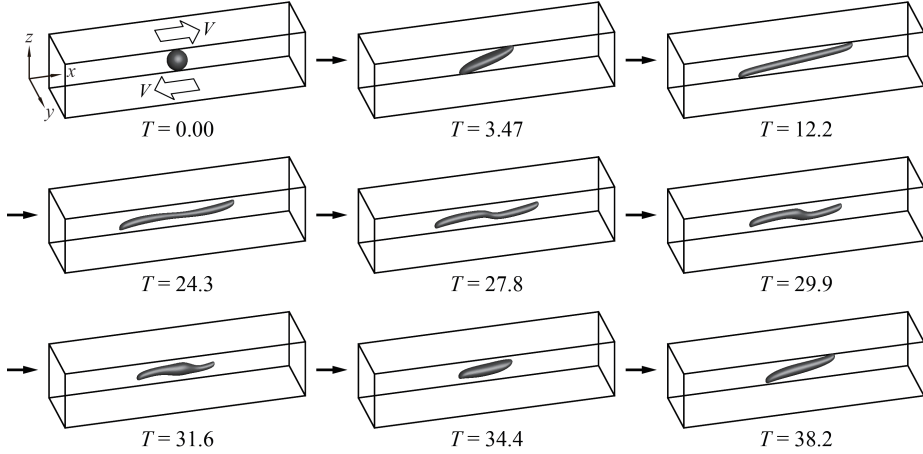


Figure 5: Time evolution of bubble deformation in shear flow at the condition of $Ca = 0.3$ and $Re = 92$. The “bubble” critical Reynolds number corresponding to $Ca = 0.3$ is $92 < Re_c < 93$. In contrast to the drop deformation case, when Re is slightly below Re_c (See Figure 4.1 $Re = 1.0$ for the drop case), the bubble shape will not reach a steady shape, instead the bubble shape alternates between the shapes “slightly stretched” ($T = 3.47$), fully stretched and “doglegged” ($T = 27.8$) and “almost” back to the original “slightly stretched” case ($T = 34.4$). ($\lambda = 1.2 \times 10^{-3}$, $\eta < 1.0 \times 10^{-3}$)

505 pinch-off; one satellite drop is also generated between the pinched-off daughter
506 drops.

507 *4.2. Bubble deformation and breakup*

508 Next, we present numerical results that illustrate the conditions that lead to
509 bubble deformation without breakup and conditions where the bubble deforms
510 and ultimately breaks up. The time evolution of shear-induced bubble defor-
511 mation without breakup at the condition of $Ca = 0.3$ and $Re = 92$ is depicted
512 in Figure 5 and the bubble breakup process with flow condition of $Ca = 0.3$
513 and $Re = 93$ is illustrated in Figure 6. The results indicate that the critical
514 Reynolds number is approximately $Re_c = 93$ (with $Ca = 0.3$). A comparison
515 with the drop breakup dynamics presented in Section 4.1 and the correspond-
516 ing processes for bubble deformation and breakup exhibit very distinct features.
517 First, we note that a relatively large shear force magnitude is required for bubble
518 breakup ($\lambda = 1.2 \times 10^{-3}$, $\eta < 1.0 \times 10^{-3}$) compared with the case of the drop (λ
519 $= \eta = 1$). Then, for the same value of $Ca = 0.3$, the critical Reynolds number
520 for the bubble is around 85 times larger than that for the drop. Focusing on the
521 bubble dynamics with no-breakup (Figure 5), the results show that the bub-
522 ble is noticeably elongated in the x -direction at the early stages ($T \leq 24.3$) of
523 bubble deformation, but the bubble does not develop the bulb-like shape (large
524 volume areas) at both ends as observed in the drop deformation process. It is
525 also evident that the ends of the deforming bubble develop cusped shapes under
526 the influence of the strong shear flow.

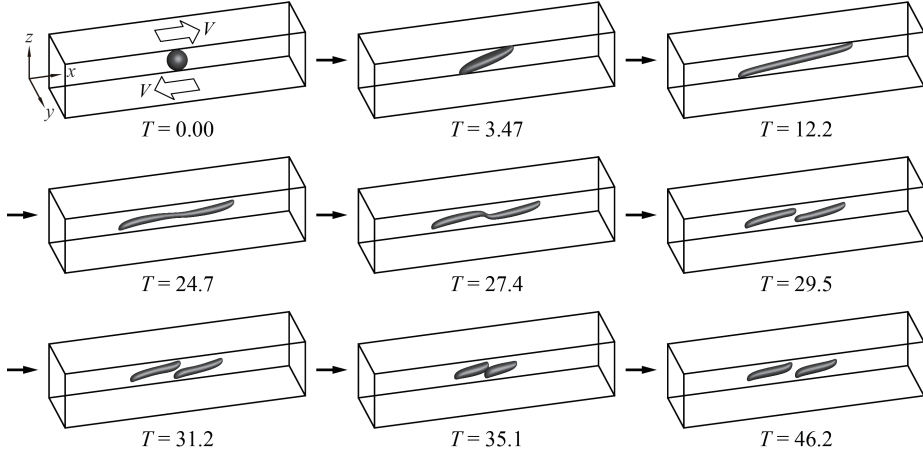


Figure 6: Time evolution of bubble deformation in shear flow at the condition of $Ca = 0.3$ and $Re = 93$. The “bubble” critical Reynolds number corresponding to $Ca = 0.3$ is $92 < Re_c < 93$. ($\lambda = 1.2 \times 10^{-3}$, $\eta < 1.0 \times 10^{-3}$)

527 In providing a more detailed description, very large shear forces are required
 528 to deform the bubble because $\lambda \simeq 0$ and $\eta \simeq 0$. Thus, the bubble undergoing
 529 large shear forces at $T > 0$ is largely stretched along the shear flow direction,
 530 and the very long elongated bubble with cusped shapes is formed. Accordingly,
 531 the bubble finally breaks up through the elongated shape without forming a
 532 bulb-like shape. A noteworthy feature of the non-breaking bubble is that it
 533 does not settle into a deformed stable state as in the case of drop deformation
 534 presented in Figure 4.1(a). After an initial elongation process, the bubble enters
 535 a shrinking phase ($T = 27.8$) where the doglegged shape formed at the center
 536 of the bubble returns to a smaller deformed shape ($T = 34.4$) that is similar to
 537 its earlier shape ($T = 3.47$). However, when we compare the early deformed
 538 bubble shape at $T = 3.47$ with the shape at $T = 34.4$, it is clear that the shapes
 539 are not identical. Following the shrinking phase, the bubble stretches again
 540 ($T = 38.2$) and oscillates between its elongated shape and shortened geometry.

541
 542 For the case of bubble breakup (Figure 6), we observe that the deformation
 543 process is almost the same as the no-breakup case until the doglegged shape
 544 is formed at $T \sim 27.4$. The bubble finally breaks during the time interval
 545 $27.7 \leq T \leq 29.5$. For a closer examination of the bubble breakup process,
 546 a detailed panel of cross-sectional slices in the xz -plane through the bubble
 547 shape center is presented in Figure 7. The images displayed in Figure 7, which
 548 are taken at shorter time intervals than those shown in Fig. 6, reveal that the
 549 bubble breaks up into two daughter bubbles due to the pinch off at the thread-
 550 bridge part of the doglegged shape during the shrinking process ($T = 28.5 \sim$
 551 28.8). After breaking up, the two daughter bubbles migrate to the center:
 552 the left daughter bubble moves toward the right side of the domain and the

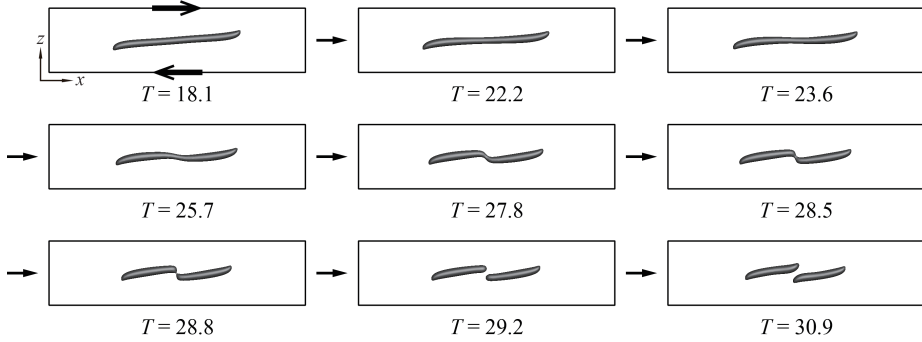


Figure 7: Detail of bubble breakup process in shear flow at the condition of $Ca = 0.3$ and $Re = 93$. The “bubble” critical Reynolds number corresponding to $Ca = 0.3$ is $92 < Re_c < 93$. ($\lambda = 1.2 \times 10^{-3}$, $\eta < 1.0 \times 10^{-3}$)

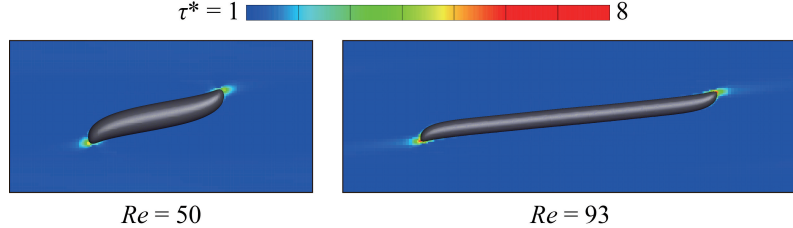


Figure 8: Normalized shear stress τ^* around a bubble for two Reynolds numbers under the condition of $Ca = 0.3$. The left image shows the shear stress profile at $Re = 50$ and the right image at $Re = 93$.

right daughter bubble moves to the left side (see results for $T = 29.5 \sim 35.1$ in Figure 6 and for $T = 28.8 \sim 30.9$ in Figure 7). The two daughter bubbles then momentarily congregate near the domain center ($T = 35.1$ in Figure 6), before they slowly start to separate: the left daughter bubble moves to the left, and the right daughter bubble moves to the right ($T = 46.2$ in Figure 6). The results demonstrate that the bubble breakup process is markedly different from the analogous drop breakup process with $\lambda = 1$ and $\eta = 1$. Note that the appearance of deformation and breakup of the drop will largely depend on the viscosity ratios.

4.3. Shear stress acting on the bubble

The previous section discussed bubble deformation and breakup. Large deformation and breakup of the bubble are expected to be closely related to the state of shear stress acting on the bubble. Figure 8 shows the shear stress profile around a bubble for two Reynolds numbers under the condition of $Ca = 0.3$: Reynolds number equal to 50 and 93. The shear stress profile on the left corresponds to the case of $Re = 50$, and the right side shows the shear stress profile for the case of $Re = 93$. The normalized shear stress, $\tau^* = \tau/\tau_0$, is defined as

570 a ratio of the local shear stress $\tau = \mu_m \sqrt{2\mathbf{D} : \mathbf{D}}$ and the apparent shear stress
 571 $\tau_0 = \mu_m \Gamma$. In this study, for a given Ca condition, the same value of τ_0 is used
 572 regardless of Re . For the case of $Re = 50$, the bubble reached a deformed stable
 573 state, and the shear stress profile around the bubble was drawn after the bubble
 574 attained a stable deformed state. As observed in previous sections, when the
 575 value of Re is slightly below the critical Re condition, the bubble does not settle
 576 into a deformed stable state. Instead, it alternates in an elongation and contrac-
 577 tion process. The shear stress profile for the case of $Re = 93$ was depicted when
 578 the bubble sufficiently elongated ($T = 14.9$). In comparison to the $Re = 50$ case
 579 on the left, the right image in Fig. 8 ($Re = 93$) shows a higher shear stress pro-
 580 file near the bubble endpoints as it undergoes an elongation state in the process
 581 toward breakup. The value of the maximum shear stress for the case of $Re = 50$
 582 is $\tau^* \approx 6$ and the maximum shear stress for the case of $Re = 93$ at the moment
 583 shown in Fig. 8 has the value of $\tau^* \approx 8$. The shear stress profile in Fig. 8 (color
 584 contour) is drawn in the range from $\tau^* = 1$ to $\tau^* = 8$, but, for emphasis, shear
 585 stress regions with $\tau^* \geq 6$ are illustrated in red. As shown in the figure, the
 586 strongest shear stresses are concentrated on the ends of the bubble for both Re
 587 conditions. This indicates that the strong shear stresses acting on the ends of
 588 the bubble are responsible for much of the bubble stretching. It is important
 589 to note that the magnitude of the shear stress acting on the ends of the bubble
 590 for the case of $Re = 93$ is much larger than that for the case of $Re = 50$.

591 We also observed that the shear stress inside the bubble was very small
 592 relative to that of the matrix fluid due to the bubble's very small density and
 593 viscosity. Since the force of strong shear stresses acting on the ends of the bubble
 594 is difficult to transfer across the interface, a sufficiently large Re condition is
 595 required for large bubble deformations.

596 In summary, we discover that for the Reynolds number sufficiently below
 597 the critical value, a relatively quick, unsteady elongation period gives way to a
 598 steady state (with no break up). On the other hand, for the Reynolds number
 599 close to the critical Reynolds number, there is a prolonged, unsteady elongation
 600 period in which periodic motion is observed, and the deformation parameter D is
 601 close to one. The "vacillating" behavior cannot last forever; ultimately (perhaps
 602 stochastically!), the bubble will either settle down or break. Regardless of the
 603 outcome, this vacillating behavior will always occur near the critical Reynolds
 604 number. In other words, irrespective of the result, we claim, using the grid
 605 resolution of $R/16$, that one is assured of being within 3 percent of the critical
 606 Reynolds number (see Figure 3). We hypothesize that there will always be
 607 "vacillating" behavior if one is sufficiently close to the critical Reynolds number.
 608 In other words, given an almost infinite supply of computational resources, as
 609 one hones in closer and closer to the critical Reynolds number, a "tug of war"
 610 will be observed between the surface tension force trying to pull the bubble
 611 together versus the wall driven shear stress trying to pull the bubble apart.

612 4.4. Velocity field outside and inside the breaking bubble

613 This section considers the fluid flow velocity field outside and inside the
 614 bubble during the shear-induced breakup process. Detailed velocity fields of

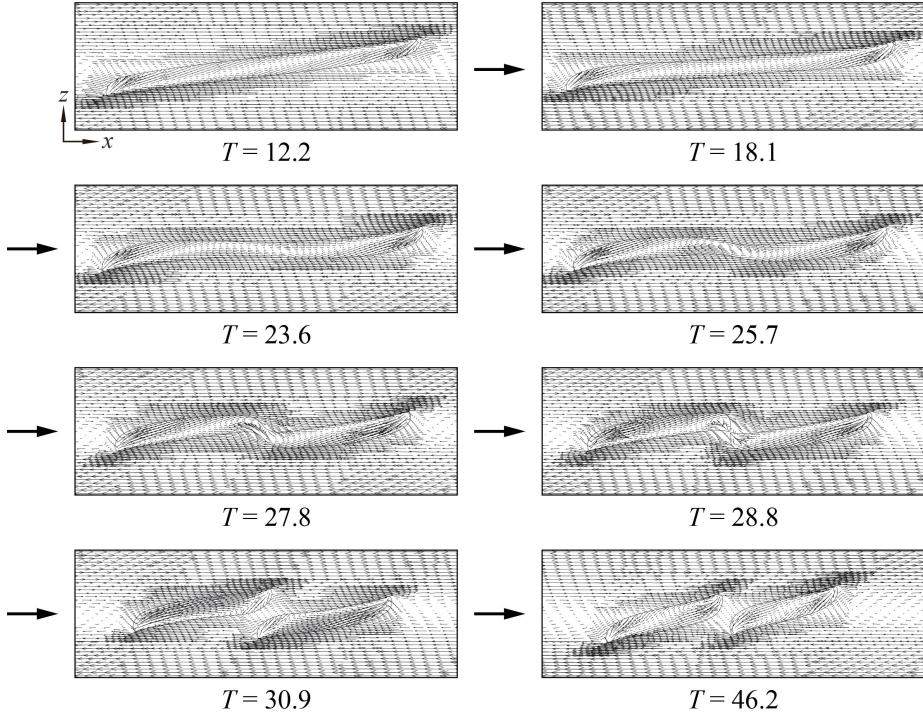


Figure 9: Fluid velocity field outside and inside the breaking bubble in shear flow at the condition $Ca = 0.3$ and $Re = 93$. The “bubble” critical Reynolds number corresponding to $Ca = 0.3$ is $92 < Re_c < 93$. ($\lambda = 1.2 \times 10^{-3}$, $\eta < 1.0 \times 10^{-3}$)

the deforming and breaking drop have already been presented in a few references (Li et al. [33], Renardy and Cristini [47]). The behavior of the breakup process will influence the velocity fields for the drop and the bubble, so the velocity fields for the drop and the bubble are not similar. Figure 9 shows the velocity fields outside and inside the bubble at cross-sectional slices in the xz -plane for a flow condition of $Ca = 0.3$ and $Re = 93$. Regions around the bubble with a higher density of velocity vectors correspond to the level-1 grid portion of the AMR structure. The simulation results show that the velocity field inside the bubble is notably distinct from the surrounding flow field on the bubble’s exterior. The cross-sections at $T = 12.2$ and $T = 18.1$, taken during the elongation phase, show how shear forces at the lower and upper halves of the bubble act along the bottom and top surfaces, respectively, to deform the interface. Near the left and right edges of the bubble, inward interior flows (that point toward the bubble center) begin to develop. Strong shearing forces in the exterior near the bottom-left-end and top-right-end of the bubble interact with the interior flow field through the boundary to create cusped shapes at the bottom-left and top-right ends of the bubble. At the same time, the interface is laterally elongated in the x -direction. During the shrinking process, which

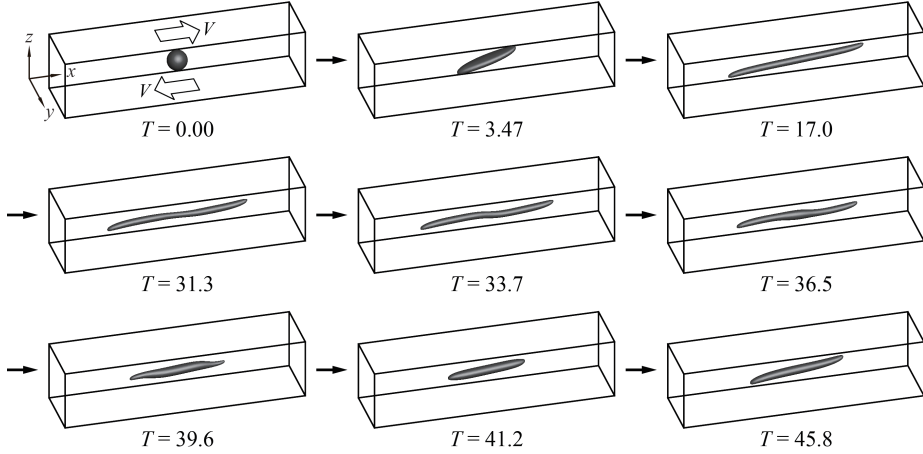


Figure 10: Time evolution of bubble deformation in shear flow at the condition of $Ca = 0.8$ and $Re = 42$. The “bubble” critical Reynolds number corresponding to $Ca = 0.8$ is $42 < Re_c < 43$. ($\lambda = 1.2 \times 10^{-3}$, $\eta < 1.0 \times 10^{-3}$)

633 occurs for $23.6 \leq T \leq 27.8$, inward flows within the bubble extend over a
 634 wider region and are no longer localized near the bubble edges. Then, we
 635 observe that circulating flows form at the thread-bridge part of the doglegged
 636 bubble shape over the time interval [25.7, 27.8]. During the breakup process
 637 ($T \sim 28.8$), higher-intensity inward flows are formed inside the bubble, near the
 638 pinch-off region, that are naturally larger than the surrounding interior flows
 639 and which are inextricably associated with the bubble migration illustrated in
 640 Figs. 6 and 7. As time proceeds further ($T = 46.2$), distinct inward flows
 641 are formed inside the daughter bubbles; the bubbles then migrate toward the
 642 side walls. For example, considering the left daughter bubble, we see that the
 643 mechanism responsible for this movement results from larger shear forces acting
 644 on the bottom-left end than those in the top-left end.

645 4.5. Effect of surface tension on bubble deformation and breakup

646 In previous sections, we considered numerical simulations of bubble deformation
 647 and breakup with a capillary number $Ca = 0.3$. In this section, we examine
 648 the case of $Ca = 0.8$. We investigate the effect of interfacial tension on bubble
 649 deformation and breakup. Using $Ca = 0.8$ for both cases, Figures 10 and 11
 650 present the time evolution of shear-induced bubble deformation and breakup
 651 with $Re = 42$ and $Re = 43$, respectively. We note that the bubble critical
 652 Reynolds number is around $Re_c \approx 43$, whereas $Re_c \approx 0$ for the corresponding
 653 case of the drop with $\lambda = \eta = 1$ (see e.g. Li et al. [33]). Note that Re_c for
 654 $Ca = 0.8$ is smaller than that for the condition of $Ca = 0.3$ since the bubble
 655 at $Ca = 0.8$ is more elastic due to the weaker effect of surface tension in this
 656 case. The results shown in Figs. 10 and 11 indicate that the bubble deforma-
 657 tion and breakup process for the condition of $Ca = 0.8$ is analogous to that for

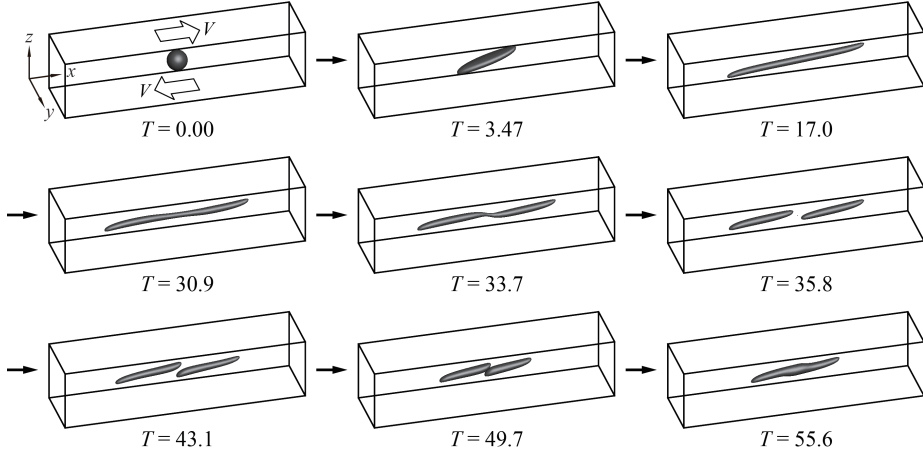


Figure 11: Time evolution of bubble deformation in shear flow at the condition of $Ca = 0.8$ and $Re = 43$. The “bubble” critical Reynolds number corresponding to $Ca = 0.8$ is $42 < Re_c < 43$. ($\lambda = 1.2 \times 10^{-3}$, $\eta < 1.0 \times 10^{-3}$)

658 $Ca = 0.3$. For the case of bubble deformation without breakup (Fig. 10), the
 659 bubble initially assumes a long elongated shape along the x -direction at around
 660 $T = 17.0$. The bubble then enters a compression stage over the time interval
 661 $[31.3, 41.2]$ and then elongates again at $T = 45.8$. On the other hand, for the
 662 case of bubble breakup (Fig. 11), an initial elongation phase is followed by a
 663 doglegged shape formation at $T = 33.7$. After that, the bubble ruptures from
 664 the thread-bridge part of the doglegged shape, producing two daughter bubbles
 665 ($T = 35.8$). The two daughter bubbles formed after the breakup move to the
 666 central area ($T = 49.7$) as in the case of $Ca = 0.8$ and $Re = 93$. Still, the two
 667 bubbles eventually coalesce in a region approximately centered in the computa-
 668 tional domain ($T = 55.6$). We note that bubbles may coalesce after breaking
 669 up in a real experimental setting due to slight deviations in flow conditions and
 670 states. Although the process of bubble deformation and breakup for flow con-
 671 ditions with $Ca = 0.3$ and $Ca = 0.8$ are similar, a pronounced difference is that
 672 the bubble for $Ca = 0.8$ is more elongated and slender than that for $Ca = 0.3$
 673 due to the smaller effect of surface tension for $Ca = 0.8$.

674 Table 4 lists, for representative Ca values, the corresponding critical Reynolds
 675 number, Re_c , for shear-induced bubble breakup. The data in Table 4 cor-
 676 responds to $\lambda = 1.2 \times 10^{-3}$, $\eta < 1.0 \times 10^{-3}$, $0.3 < Ca < 1$, and the ini-
 677 tial/boundary conditions are given by (1). The results in Table 4 indicate that
 678 sufficiently large shear forces are required for bubble breakup, even for large
 679 capillary numbers. In Figure 12 we plot the smooth interpolant of the data
 680 given in Table 4 and make the hypothesis that given a new data point, (Ca, Re) ,
 681 shear-induced bubble break up will occur if the point (Ca, Re) is above the given
 682 critical curve, and the bubble will not break if the (Ca, Re) pair is below the crit-
 683 ical curve. For comparison, a critical curve for the drop with $\lambda = \eta = 1$ is also

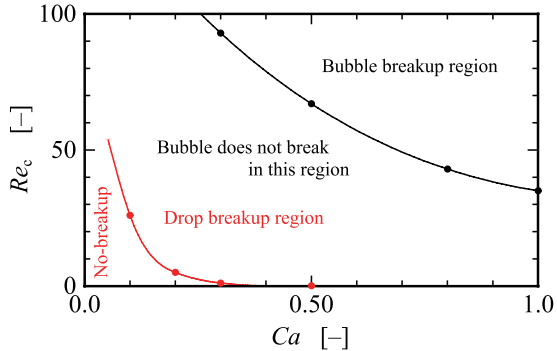


Figure 12: A plot of the critical Reynolds number versus capillary number for the data listed in Table 4. $\lambda = 1.2 \times 10^{-3}$, $\eta < 1.0 \times 10^{-3}$, $0.3 < Ca < 1$, and the initial/boundary conditions are given by (1). Given a new data point, (Ca, Re) , one can reliably predict whether the given (Ca, Re) pair will result in shear induced bubble breakup or not. Note, for the “Drop delineation curve,” $\lambda = \eta = 1$.

684 indicated in Fig. 12. Including breakup and no-breakup critical curves for both
 685 the drop and the bubble will facilitate future identification of Re_c numbers and,
 686 thus, a complete general critical curve for a wide range of Ca numbers.

Table 4: Shear-induced bubble breakup for various flow conditions described in terms of column pairs of critical Reynolds numbers and corresponding capillary numbers. ($\lambda = 1.2 \times 10^{-3}$, $\eta < 1.0 \times 10^{-3}$)

Capillary number Ca	0.3	0.5	0.8	1.0
Critical Reynolds number Re_c	93	67	43	35

687 5. Conclusions

688 The bubble deformation and breakup process in liquid due to a driving
 689 simple linear shear flow was explored numerically using the CLSVOF compu-
 690 tational method. In this study, the critical Reynolds number Re_c , at which
 691 bubble breakup first occurs, was determined for several flow conditions, and the
 692 differences between the morphology of bubble deformation and breakup were
 693 compared with the analogous morphology of drop deformation and breakup.

694 The numerical results revealed significant differences between bubble de-
 695 formation and breakup and the corresponding drop dynamics. For the case
 696 of a bubble, it was discovered that much stronger shear flows are necessary
 697 to induce interface breakup compared with a drop immersed in a similar flow
 698 field. That is, a much larger Reynolds number flow is required to induce bubble
 699 breakup. The steps leading to bubble breakup were similar throughout the Ca
 700 number range considered in our computations: the bubble underwent a simi-
 701 lar breakup mechanism in which rupture occurred at a thread-bridge part that

702 followed a doglegged shape formation stage. For bubble deformation without
703 breakup, near Re_c , the bubble did not maintain a stable deformed shape, unlike
704 drop deformation near the critical Reynolds number. The bubble exhibited pro-
705 nounced underdamped behavior: the bubble oscillated between elongating and
706 shrinking motions for non-rupturing flow conditions. At the same time, bubble
707 deformation under smaller Re conditions ($< Re_c$) led to a stable state. Com-
708 pared with the drop, we attribute the significant differences in morphology for
709 the bubble undergoing breakup to the density and viscosity ratio. Due to the
710 bubble's very small density and viscosity, it is comparatively difficult to transfer
711 the shear stresses acting on the ends of the bubble across the interface.

712 There are several directions for future work. In the present work, we varied
713 the capillary number and Reynolds number to study bubble deformation and
714 breakup morphology in the presence of a simple shear flow. For the future,
715 one can also vary (i) the viscosity ratio, (ii) the effect of the initial shape of
716 the bubble[39], (iii) the magnitude and direction of the gravitational force, (iv)
717 the non-Newtonian properties of the “matrix” liquid, (v) bubble deformation
718 and breakup due to a shear flow in a T junction[16], (vi) bubble deformation
719 and breakup confined shear flow (see [18] for the drop case), and (vii) bubble
720 deformation and breakup due to non-uniform shear flow (see [6] for the drop
721 case).

722 References

- 723 [1] Amani, A., Balcázar, N., Castro, J., Oliva, A., 2019. Numerical study of droplet deformation in shear flow using a con-
724 servative level-set method. Chemical Engineering Science 207,
725 153–171. URL: <http://www.sciencedirect.com/science/article/pii/S0009250919305123>, doi:<https://doi.org/10.1016/j.ces.2019.06.014>.
- 726 [2] Arienti, M., Li, X., Soteriou, M., Eckett, C., Sussman, M., Jensen, R., 2013. Coupled level-set/volume-of-fluid method for simulation of injector
727 atomization. Journal of propulsion and power 29, 147–157.
- 728 [3] Bazhlekov, I.B., Anderson, P.D., Meijer, H.E., 2006. Numerical investi-
729 gation of the effect of insoluble surfactants on drop deformation and
730 breakup in simple shear flow. Journal of Colloid and Interface Sci-
731 ence 298, 369 – 394. URL: <http://www.sciencedirect.com/science/article/pii/S0021979705012658>, doi:<http://dx.doi.org/10.1016/j.jcis.2005.12.017>.
- 732 [4] Bento, D., Rodrigues, R.O., Faustino, V., Pinho, D., Fernandes, C.S.,
733 Pereira, A.I., Garcia, V., Miranda, J.M., Lima, R., 2018. Deforma-
734 tion of red blood cells, air bubbles, and droplets in microfluidic devices:
735 Flow visualizations and measurements. Micromachines 9, 151. URL:
736 <https://www.mdpi.com/2072-666X/9/4/151>, doi:[10.3390/mi9040151](https://doi.org/10.3390/mi9040151).

- 743 [5] Canedo, E.L., Favelukis, M., Tadmor, Z., Talmon, Y., 1993.
744 An experimental study of bubble deformation in viscous liq-
745 uids in simple shear flow. *AIChE Journal* 39, 553–559. URL:
746 <https://aiche.onlinelibrary.wiley.com/doi/abs/10.1002/aic.690390403>,
747 doi:<https://doi.org/10.1002/aic.690390403>,
748 arXiv:<https://aiche.onlinelibrary.wiley.com/doi/pdf/10.1002/aic.690390403>.
- 749 [6] Chin, H.B., Han, C.D., 1980. Studies on droplet deformation and breakup.
750 ii. breakup of a droplet in nonuniform shear flow. *Journal of rheology* 24,
751 1–37.
- 752 [7] Chu, P., Finch, J., Bournival, G., Ata, S., Hamlett, C., Pugh, R.J.,
753 2019. A review of bubble break-up. *Advances in Colloid and In-*
754 *terface Science* 270, 108–122. URL: <https://www.sciencedirect.com/science/article/pii/S0001868619300211>, doi:<https://doi.org/10.1016/j.cis.2019.05.010>.
- 755 [8] Cristini, V., Bławdziewicz, J., Loewenberg, M., 2001. An adap-
756 tive mesh algorithm for evolving surfaces: simulations of drop breakup
757 and coalescence. *Journal of Computational Physics* 168, 445 –
758 463. URL: <http://www.sciencedirect.com/science/article/pii/S0021999101967130>, doi:<http://dx.doi.org/10.1006/jcph.2001.6713>.
- 759 [9] Cristini, V., Guido, S., Alfani, A., Bławdziewicz, J., Loewenberg, M.,
760 2003. Drop breakup and fragment size distribution in shear flow. *Journal*
761 *of Rheology* 47, 1283–1298. URL: <http://scitation.aip.org/content/sor/journal/jor2/47/5/10.1122/1.1603240>, doi:<http://dx.doi.org/10.1122/1.1603240>.
- 762 [10] Croce, R., Griebel, M., Schweitzer, M.A., 2010. Numerical simulation of
763 bubble and droplet deformation by a level set approach with surface tension
764 in three dimensions. *International Journal for Numerical Methods in Fluids*
765 62, 963–993. URL: <http://dx.doi.org/10.1002/fld.2051>, doi:<10.1002/fld.2051>.
- 766 [11] Drenckhan, W., Saint-Jalmes, A., 2015. The science of foaming. *Ad-*
767 *vances in Colloid and Interface Science* 222, 228–259. URL: <https://www.sciencedirect.com/science/article/pii/S0001868615000603>,
768 doi:<https://doi.org/10.1016/j.cis.2015.04.001>. reinhard Miller,
769 Honorary Issue.
- 770 [12] Eftekhari, M., Schwarzenberger, K., Heitkam, S., Eckert, K.,
771 2021a. Interfacial flow of a surfactant-laden interface under asym-
772 metric shear flow. *Journal of Colloid and Interface Science* 599,
773 837–848. URL: <https://www.sciencedirect.com/science/article/pii/S0021979721006457>, doi:<https://doi.org/10.1016/j.jcis.2021.04.126>.

- 783 [13] Eftekhari, M., Schwarzenberger, K., Heitkam, S., Javadi, A.,
784 Bashkatov, A., Ata, S., Eckert, K., 2021b. Interfacial be-
785 havior of particle-laden bubbles under asymmetric shear flow.
786 Langmuir 37, 13244–13254. URL: <https://doi.org/10.1021/acs.langmuir.1c01814>,
787 doi:10.1021/acs.langmuir.1c01814, arXiv:<https://doi.org/10.1021/acs.langmuir.1c01814>. pMID:
788 34726918.
- 790 [14] Ervin, E., Tryggvason, G., 1997. The rise of bubbles in a vertical shear
791 flow. Journal of Fluids Engineering 119(2), 443–449.
- 792 [15] Fang, Z., Shuai, Y., Huang, Z., Wang, J., Yang, Y., 2024. Inten-
793 sification of polyethylene devolatilization in twin-screw extruder
794 with additives. Polymer Engineering & Science 64, 2961–2974.
795 URL: <https://4sceppublications.onlinelibrary.wiley.com/doi/abs/10.1002/pen.26738>,
796 doi:<https://doi.org/10.1002/pen.26738>, arXiv:<https://4sceppublications.onlinelibrary.wiley.com/doi/pdf/10.1002/pen.26738>.
- 798 [16] Frense, E., Rüdiger, F., Fröhlich, J., 2024. Modeling of dynamic bub-
799 ble deformation and breakup in t-junction channel flow. Chemical En-
800 gineering Science 300, 120579. URL: <https://www.sciencedirect.com/science/article/pii/S0009250924008790>, doi:<https://doi.org/10.1016/j.ces.2024.120579>.
- 803 [17] Gao, S., Shi, Y., Pan, G., Quan, X., 2022. Research on the
804 effect of asymmetric bubbles on the load characteristics of projec-
805 tiles during an underwater salvo. Applied Ocean Research 124,
806 103212. URL: <https://www.sciencedirect.com/science/article/pii/S0141118722001535>, doi:<https://doi.org/10.1016/j.apor.2022.103212>.
- 809 [18] Gupta, A., Sbragaglia, M., 2014. Deformation and breakup of viscoelastic
810 droplets in confined shear flow. Physical Review E 90, 023305.
- 811 [19] Hernandez, F.H., Rangel, R.H., 2017. Breakup of drops in simple
812 shear flows with high-confinement geometry. Computers & Fluids 146,
813 23 – 41. URL: <http://www.sciencedirect.com/science/article/pii/S0045793017300038>, doi:<https://doi.org/10.1016/j.compfluid.2017.01.001>.
- 816 [20] Hirt, C., Nichols, B., 1981. Volume of fluid (vof) method
817 for the dynamics of free boundaries. Journal of Computational
818 Physics 39, 201 – 225. URL: <http://www.sciencedirect.com/science/article/pii/0021999181901455>, doi:[http://dx.doi.org/10.1016/0021-9991\(81\)90145-5](http://dx.doi.org/10.1016/0021-9991(81)90145-5).
- 821 [21] Hoyt, N.C., 2013. The performance of passive cyclonic separators in mi-
822 crogravity. Case Western Reserve University.

- 823 [22] Inamuro, T., 2006. Lattice boltzmann methods for viscous fluid flows and
824 for two-phase fluid flows. *Fluid Dynamics Research* 38, 641. URL: <http://stacks.iop.org/1873-7005/38/i=9/a=A04>.
- 826 [23] Inamuro, T., Tomita, R., Ogino, F., 2003. Lattice boltzmann simulations of drop deformation and breakup in simple shear flows. *International Journal of Modern Physics B* 17, 21–26. URL: <http://www.worldscientific.com/doi/abs/10.1142/S0217979203017035>, doi:10.1142/S0217979203017035.
- 831 [24] Ioannou, N., Liu, H., Zhang, Y., 2016. Droplet dynamics
832 in confinement. *Journal of Computational Science* 17, 463 –
833 474. URL: <http://www.sciencedirect.com/science/article/pii/S1877750316300308>, doi:<https://doi.org/10.1016/j.jocs.2016.03.009>. *discrete Simulation of Fluid Dynamics* 2015.
- 836 [25] Janssen, P., Anderson, P., 2008. A boundary-integral model for
837 drop deformation between two parallel plates with non-unit viscosity
838 ratio drops. *Journal of Computational Physics* 227, 8807–
839 8819. URL: <http://www.sciencedirect.com/science/article/pii/S002199910800346X>, doi:<http://dx.doi.org/10.1016/j.jcp.2008.06.027>.
- 842 [26] Janssen, P.J.A., Anderson, P.D., 2007. Boundary-integral method
843 for drop deformation between parallel plates. *Physics of Fluids*
844 19. URL: <http://scitation.aip.org/content/aip/journal/pof2/19/4/10.1063/1.2715621>, doi:<http://dx.doi.org/10.1063/1.2715621>.
- 846 [27] Kang, M., Fedkiw, R.P., Liu, X.D., 2000. A boundary condition capturing
847 method for multiphase incompressible flow. *Journal of scientific computing*
848 15, 323–360.
- 849 [28] Khismatullin, D.B., Renardy, Y., Cristini, V., 2003. Inertia-induced
850 breakup of highly viscous drops subjected to simple shear. *Physics of Fluids*
851 15, 1351–1354. doi:<http://dx.doi.org/10.1063/1.1564825>.
- 852 [29] Komrakova, A., Shardt, O., Eskin, D., Derksen, J., 2014. Lattice
853 boltzmann simulations of drop deformation and breakup in shear flow.
854 *International Journal of Multiphase Flow* 59, 24 – 43. URL: <http://www.sciencedirect.com/science/article/pii/S0301932213001547>,
855 doi:<http://dx.doi.org/10.1016/j.ijmultiphaseflow.2013.10.009>.
- 857 [30] Komrakova, A., Shardt, O., Eskin, D., Derksen, J., 2015. Effects
858 of dispersed phase viscosity on drop deformation and breakup
859 in inertial shear flow. *Chemical Engineering Science* 126, 150 –
860 159. URL: <http://www.sciencedirect.com/science/article/pii/S000925091400726X>, doi:<http://dx.doi.org/10.1016/j.ces.2014.12.012>.

- 863 [31] Legendre, D., Magnaudet, J., 1998. The lift force on a spherical bubble in
864 a viscous linear shear flow. *Journal of Fluid Mechanics* 368, 81–126.
- 865 [32] Lewin-Jones, P., Lockerby, D.A., Sprittles, J.E., 2024. Collision of liquid
866 drops: bounce or merge? *Journal of Fluid Mechanics* 995, A1. doi:10.
867 1017/jfm.2024.722.
- 868 [33] Li, J., Renardy, Y., Renardy, M., 2000. Numerical simulation of
869 breakup of a viscous drop in simple shear flow through a volume-of-fluid
870 method. *Physics of Fluids* 12, 269–282. URL: <http://scitation.aip.org/content/aip/journal/pof2/12/2/10.1063/1.870305>, doi:<http://dx.doi.org/10.1063/1.870305>.
- 873 [34] Li, X., Soteriou, M.C., 2016. High fidelity simulation and analysis of liq-
874 uid jet atomization in a gaseous crossflow at intermediate weber numbers.
875 *Physics of Fluids* 28.
- 876 [35] Lohse, D., 2018. Bubble puzzles: from fundamentals to applications. *Phys-
877 ical review fluids* 3, 110504.
- 878 [36] Müller-Fischer, N., Tobler, P., Dressler, M., Fischer, P., Windhab, E.J.,
879 2008. Single bubble deformation and breakup in simple shear flow. *Experi-
880 ments in fluids* 45, 917–926.
- 881 [37] Ohta, M., Akama, Y., Yoshida, Y., Sussman, M., 2014. Influence of the
882 viscosity ratio on drop dynamics and breakup for a drop rising in an im-
883 miscible low-viscosity liquid. *Journal of Fluid Mechanics* 752, 383–409.
884 doi:10.1017/jfm.2014.339.
- 885 [38] Ohta, M., Furukawa, T., Yoshida, Y., Sussman, M., 2019. A
886 three-dimensional numerical study on the dynamics and deformation
887 of a bubble rising in a hybrid carreau and fene-cr modeled poly-
888 mERIC liquid. *Journal of Non-Newtonian Fluid Mechanics* 265, 66–
889 78. URL: <https://www.sciencedirect.com/science/article/pii/S0377025718301952>, doi:<https://doi.org/10.1016/j.jnnfm.2018.12.012>.
- 892 [39] Ohta, M., Imura, T., Yoshida, Y., Sussman, M., 2005. A computational
893 study of the effect of initial bubble conditions on the motion of a gas bubble
894 rising in viscous liquids. *International journal of multiphase flow* 31, 223–
895 237.
- 896 [40] Ohta, M., Kikuchi, D., Yoshida, Y., Sussman, M., 2011. Robust numeri-
897 cal analysis of the dynamic bubble formation process in a viscous liquid.
898 *International Journal of Multiphase Flow* 37, 1059–1071.
- 899 [41] Ohta, M., Sussman, M., 2012. The buoyancy-driven mo-
900 tion of a single skirted bubble or drop rising through
901 a viscous liquid. *Physics of Fluids* 24, 112101. URL:

- 902 <https://doi.org/10.1063/1.4765669>, doi:10.1063/1.4765669,
 903 arXiv:https://pubs.aip.org/aip/pof/article-pdf/doi/10.1063/1.4765669/14128560/112101_1.pdf
- 904 [42] Ohta, M., Yamaguchi, S., Yoshida, Y., Sussman, M., 2010. The sensitivity
 905 of drop motion due to the density and viscosity ratio. Physics of Fluids 22.
- 906 [43] Rallison, J.M., 1984. The deformation of small viscous drops
 907 and bubbles in shear flows. Annual Review of Fluid Mechanics 16, 45–66. URL: <http://dx.doi.org/10.1146/annurev.fl.16.010184.000401>,
 909 doi:10.1146/annurev.fl.16.010184.000401,
 910 arXiv:<http://dx.doi.org/10.1146/annurev.fl.16.010184.000401>.
- 911 [44] Renardy, Y., 2006. Numerical simulation of a drop undergoing large am-
 912 plitude oscillatory shear. Rheologica acta 45, 223–227.
- 913 [45] Renardy, Y., 2007. The effects of confinement and inertia on the production
 914 of droplets. Rheologica Acta 46, 521–529. URL: <http://dx.doi.org/10.1007/s00397-006-0150-y>, doi:10.1007/s00397-006-0150-y.
- 916 [46] Renardy, Y., 2008. Effect of startup conditions on drop breakup
 917 under shear with inertia. International Journal of Multiphase Flow 34, 1185 – 1189. URL: <http://www.sciencedirect.com/science/article/pii/S030193220800089X>, doi:<http://dx.doi.org/10.1016/j.ijmultiphaseflow.2008.04.004>.
- 921 [47] Renardy, Y., Cristini, V., 2001a. Effect of inertia on drop breakup under
 922 shear. Physics of Fluids 13, 7–13. URL: <http://scitation.aip.org/content/aip/journal/pof2/13/1/10.1063/1.1331321>, doi:<http://dx.doi.org/10.1063/1.1331321>.
- 925 [48] Renardy, Y., Cristini, V., Li, J., 2002. Drop fragment distributions un-
 926 der shear with inertia. International Journal of Multiphase Flow 28, 1125
 927 – 1147. URL: <http://www.sciencedirect.com/science/article/pii/S0301932202000228>, doi:[http://dx.doi.org/10.1016/S0301-9322\(02\)00022-8](http://dx.doi.org/10.1016/S0301-9322(02)00022-8).
- 930 [49] Renardy, Y.Y., Cristini, V., 2001b. Scalings for fragments produced
 931 from drop breakup in shear flow with inertia. Physics of Fluids 13,
 932 2161–2164. URL: <https://doi.org/10.1063/1.1384469>, doi:10.1063/
 933 1.1384469, arXiv:<https://doi.org/10.1063/1.1384469>.
- 934 [50] Rust, A., Manga, M., 2002. Bubble shapes and orientations in low re-
 935 simple shear flow. Journal of Colloid and Interface Science 249, 476–
 936 480. URL: <https://www.sciencedirect.com/science/article/pii/S0021979702982925>, doi:<https://doi.org/10.1006/jcis.2002.8292>.
- 938 [51] Sanogo, B., Souidi, K., Marcati, A., Vial, C., 2023. Food aeration: Ef-
 939 fect of the surface-active agent type on bubble deformation and break-up
 940 in a viscous newtonian fluid: From single bubble to process-scale. Food

- 941 Research International 165, 112478. URL: <https://www.sciencedirect.com/science/article/pii/S0963996923000236>, doi:<https://doi.org/10.1016/j.foodres.2023.112478>.
- 944 [52] Schlüter, M., Herres-Pawlis, S., Nieken, U., Tuttles, U., Bothe, D., 2021. 945 Small-scale phenomena in reactive bubbly flows: Experiments, numerical 946 modeling, and applications. Annual review of chemical and biomolecular 947 engineering 12, 625–643.
- 948 [53] Sharifi, R., Varmazyar, M., Mohammadi, A., 2024. Investigating 949 droplet and bubble deformation under shear flow using the multi-pseudo-potential scheme of lattice boltzmann 950 method. Advances in Applied Mathematics and Mechanics 16, 519–548. URL: <https://global-sci.com/article/72820/investigating-droplet-and-bubble-deformation-under-shear-flow-using-the-multi-pseudo-potential-scheme-of-lattice-boltzmann-method>, doi:<https://doi.org/10.4208/aamm.OA-2021-0326>.
- 955 [54] Sines, J.N., Straiton, B.J., Zuccarelli, C.E., Marashdeh, Q.M., Teixeira, F.L., Fan, L.S., Motil, B.J., 2020. Study of gas-water flow inside 956 of a horizontal passive cyclonic gas-liquid phase separator system using 957 displacement-current phase tomography. Gravitational and Space Research 958 6, 28–43.
- 959 [55] Stewart, P., Lay, N., Sussman, M., Ohta, M., 2008. An improved sharp 960 interface method for viscoelastic and viscous two-phase flows. Journal of 961 Scientific Computing 35, 43–61.
- 962 [56] Stone, H.A., 1994. Dynamics of drop deformation and breakup 963 in viscous fluids. Annual Review of Fluid Mechanics 26, 964 65–102. URL: <http://dx.doi.org/10.1146/annurev.fl.26.010194.000433>, 965 doi:<https://doi.org/10.1146/annurev.fl.26.010194.000433>, arXiv:<http://dx.doi.org/10.1146/annurev.fl.26.010194.000433>.
- 966 [57] Sussman, M., 2003. A second order coupled level set and volume-of-fluid 967 method for computing growth and collapse of vapor bubbles. Journal of Computational Physics 187, 110–136. URL: <https://www.sciencedirect.com/science/article/pii/S0021999103000871>, 968 doi:[https://doi.org/10.1016/S0021-9991\(03\)00087-1](https://doi.org/10.1016/S0021-9991(03)00087-1).
- 969 [58] Sussman, M., Almgren, A.S., Bell, J.B., Colella, P., Howell, L.H., 970 Welcome, M.L., 1999. An adaptive level set approach for incompressible 971 two-phase flows. Journal of Computational Physics 148, 81–124. URL: <http://www.sciencedirect.com/science/article/pii/S002199919896106X>, 972 doi:<https://doi.org/10.1006/jcph.1998.6106>.
- 973 [59] Sussman, M., Ohta, M., 2009. A stable and efficient method for treating 974 surface tension in incompressible two-phase flow. SIAM Journal on 975 Scientific Computing 31, 2447–2471.
- 976

- 981 [60] Sussman, M., Puckett, E.G., 2000. A coupled level set and
 982 volume-of-fluid method for computing 3d and axisymmetric incompress-
 983ible two-phase flows. *Journal of Computational Physics* 162, 301–
 984 337. URL: <http://www.sciencedirect.com/science/article/pii/S0021999100965379>, doi:<http://dx.doi.org/10.1006/jcph.2000.6537>.
- 986 [61] Sussman, M., Smereka, P., Osher, S., 1994. A level set ap-
 987 proach for computing solutions to incompressible two-phase flow.
 988 *Journal of Computational Physics* 114, 146 – 159. URL: <http://www.sciencedirect.com/science/article/pii/S0021999184711557>,
 990 doi:<http://dx.doi.org/10.1006/jcph.1994.1155>.
- 991 [62] Sussman, M., Smith, K., Hussaini, M., Ohta, M., Zhi-Wei, R., 2007. A
 992 sharp interface method for incompressible two-phase flows. *Journal of Com-
 993 putational Physics* 221, 469–505. URL: <https://www.sciencedirect.com/science/article/pii/S0021999106002981>, doi:<https://doi.org/10.1016/j.jcp.2006.06.020>.
- 996 [63] Tanguy, S., Ménard, T., Berlemont, A., 2007. A level set method for
 997 vaporizing two-phase flows. *Journal of Computational Physics* 221, 837–
 998 853.
- 999 [64] Tatebe, O., 1993. The multigrid preconditioned conjugate gradient method,
 1000 in: NASA. Langley Research Center, The Sixth Copper Mountain Confer-
 1001ence on Multigrid Methods, Part 2.
- 1002 [65] Taylor, G.I., 1932. The viscosity of a fluid containing small drops of another
 1003 fluid. *Proceedings of the Royal Society of London A: Mathematical, Phys-
 1004 ical and Engineering Sciences* 138, 41–48. doi:<10.1098/rspa.1932.0169>.
- 1005 [66] Taylor, G.I., 1934. The formation of emulsions in definable fields of flow.
 1006 *Proceedings of the Royal Society of London A: Mathematical, Physical and
 1007 Engineering Sciences* 146, 501–523. doi:<10.1098/rspa.1934.0169>.
- 1008 [67] Unverdi, S.O., Tryggvason, G., 1992. A front-tracking method
 1009 for viscous, incompressible, multi-fluid flows. *Journal of Computa-
 1010 tional Physics* 100, 25 – 37. URL: <http://www.sciencedirect.com/science/article/pii/002199919290307K>, doi:[http://dx.doi.org/10.1016/0021-9991\(92\)90307-K](http://dx.doi.org/10.1016/0021-9991(92)90307-K).
- 1013 [68] Wang, A., Evans, G., Mitra, S., 2023. A review of bubble
 1014 surface loading and its effect on bubble dynamics. *Miner-
 1015 als Engineering* 199, 108105. URL: <https://www.sciencedirect.com/science/article/pii/S089268752300119X>, doi:<https://doi.org/10.1016/j.mineng.2023.108105>.
- 1018 [69] Wang, Z., Shi, D., Zhang, A., 2015. Three-dimensional lattice boltz-
 1019 man simulation of bubble behavior in a flap-induced shear flow. *Com-
 1020 puters & Fluids* 123, 44 – 53. URL: <http://www.sciencedirect.com>

- 1021 com/science/article/pii/S0045793015003199, doi:<https://doi.org/10.1016/j.compfluid.2015.09.007>.

1022

1023 [70] Wei, Y.K., Qian, Y., Xu, H., 2012. Lattice boltzmann simulations
1024 of single bubble deformation and breakup in a shear flow. The Journal
1025 of Computational Multiphase Flows 4, 111–117. URL: <https://doi.org/10.1260/1757-482X.4.1.111>, doi:<https://doi.org/10.1260/1757-482X.4.1.111>, arXiv:<https://doi.org/10.1260/1757-482X.4.1.111>.

1026

1027

1028 [71] Wong, A., Park, C., 2012. A visualization system for observing
1029 plastic foaming processes under shear stress. Polymer Testing
1030 31, 417–424. URL: <https://www.sciencedirect.com/science/article/pii/S0142941811002169>, doi:<https://doi.org/10.1016/j.polymertesting.2011.12.012>.

1031

1032

1033 [72] Yoshikawa, H.N., Zoueshtiagh, F., Caps, H., Kurowski, P., Petitjeans, P.,
1034 2010. Bubble splitting in oscillatory flows on ground and in reduced gravity.
1035 The European Physical Journal E 31, 191–199.

1036

1037

1038 [73] Zhang, J., Miksis, M.J., Bankoff, S.G., 2006. Nonlinear dynamics of
1039 a two-dimensional viscous drop under shear flow. Physics of Fluids
18. URL: <http://scitation.aip.org/content/aip/journal/pof2/18/7/10.1063/1.2222336>, doi:<http://dx.doi.org/10.1063/1.2222336>.

1040

1041 [74] Zhang, J., Ni, M.J., Magnaudet, J., 2021a. Three-dimensional dynamics
1042 of a pair of deformable bubbles rising initially in line. part 1. moderately
1043 inertial regimes. Journal of Fluid Mechanics 920, A16.

1044

1045 [75] Zhang, J., Ni, M.J., Magnaudet, J., 2022. Three-dimensional dynamics of
1046 a pair of deformable bubbles rising initially in line. part 2. highly inertial
1047 regimes. Journal of Fluid Mechanics 943, A10.

1048

1049 [76] Zhang, J., Shu, S., Guan, X., Yang, N., 2021b. Regime map-
1050 ping of multiple breakup of droplets in shear flow by phase-field
1051 lattice boltzmann simulation. Chemical Engineering Science 240,
116673. URL: <https://www.sciencedirect.com/science/article/pii/S0009250921002384>, doi:<https://doi.org/10.1016/j.ces.2021.116673>.

1052

1053 [77] Zhang, W., Almgren, A., Beckner, V., Bell, J., Blaschke, J., Chan, C.,
1054 Day, M., Friesen, B., Gott, K., Graves, D., Katz, M., Myers, A., Nguyen,
1055 T., Nonaka, A., Rosso, M., Williams, S., Zingale, M., 2019. AMReX: a
1056 framework for block-structured adaptive mesh refinement. Journal of Open
1057 Source Software 4, 1370. URL: <https://doi.org/10.21105/joss.01370>,
doi:<https://doi.org/10.21105/joss.01370>.